

# A simple polarizable continuum solvation model for electrolyte solutions

Adrian W. Lange and John M. Herbert<sup>a)</sup>*Department of Chemistry, The Ohio State University, Columbus, Ohio 43210, USA*

(Received 28 January 2011; accepted 29 April 2011; published online 26 May 2011)

We propose a Debye-Hückel-like screening model (DESMO) that generalizes the familiar conductor-like screening model (COSMO) to solvents with non-zero ionic strength and furthermore provides a numerical generalization of the Debye-Hückel model that is applicable to non-spherical solute cavities. The numerical implementation of DESMO is based upon the switching/Gaussian (SWIG) method for smooth cavity discretization, which we have recently introduced in the context of polarizable continuum models (PCMs). This approach guarantees that the potential energy is a smooth function of the solute geometry and analytic gradients for DESMO are reported here. The SWIG formalism also facilitates analytic implementation of two other PCMs that are based on a screened Coulomb potential: the “integral equation formalism” (IEF-PCM) and the “surface and simulation of volume polarization for electrostatics” [SS(V)PE] method. Fully analytic implementations of these screened PCMs are reported here for the first time. Numerical results, for model systems where an exact solution of the linearized Poisson-Boltzmann equation is available, demonstrate that these screened PCMs are highly accurate. In realistic test cases, they are as accurate as the best available three-dimensional finite-difference methods. In polar solvents, DESMO is nearly as accurate as more sophisticated screened PCMs, but is significantly simpler and more efficient. © 2011 American Institute of Physics. [doi:10.1063/1.3592372]

## I. INTRODUCTION

Implicit solvent models play an important role in both biomolecular simulations<sup>1–14</sup> and quantum chemistry calculations.<sup>15–20</sup> These models dramatically enhance conformational sampling and also reduce the complexity of free energy calculations, as compared to simulations using explicit, atomistic representations of the solvent. A wide variety of implicit solvent models have been introduced over the years, ranging from microscopic to semi-microscopic to macroscopic<sup>7,21,22</sup> and varying widely in their level of sophistication. The merits of—and problems associated with—many of these approaches have been discussed in recent reviews.<sup>4–13,17,19</sup> The present work introduces a new implicit solvent model for electrolyte solutions that allows for variation of the solute geometry and provides smooth forces for molecular dynamics simulations, for arbitrary cavity shapes.

Specifically, we focus on solution of the classical electrostatic continuum problem (Poisson’s equation) modified by the presence of a thermal distribution of mobile ions. The electrostatic interaction between two different dielectrics, or the interaction between a dielectric continuum and an atomistic region, is then described by the Poisson-Boltzmann equation.<sup>6,8,9</sup> Truncating Boltzmann factors at first order, one obtains the *linearized* Poisson-Boltzmann equation (LPBE),<sup>23</sup>

$$(\hat{\nabla}^2 - \kappa^2)U(\vec{r}) = 0, \quad (1.1)$$

which is also known as the *Debye-Hückel equation*. The quantity  $U(\vec{r})$  represents the electrostatic potential. Within the LPBE, the solvent is characterized by a dielectric constant

(relative permittivity),  $\epsilon$ , and a Debye length  $\lambda = \kappa^{-1}$ , where

$$\kappa = \frac{1}{\lambda} = \left( \frac{8\pi e^2 \mathcal{J}}{\epsilon k_B T} \right)^{1/2}. \quad (1.2)$$

The quantity  $\lambda$  characterizes the length scale on which the mobile ions screen the Coulomb potential. This length scale depends upon the *ionic strength* of the solution,

$$\mathcal{J} = \frac{1}{2} \sum_i z_i^2 c_i. \quad (1.3)$$

The sum in this equation ranges over dissolved ionic species with concentrations  $c_i$  and dimensionless charge numbers  $z_i$ .

Equation (1.1) forms the basis of the electrostatic solvation effects that we wish to describe. We consider an atomistic representation of the solute molecule(s) and a continuum description of the solvent, the latter parameterized by  $\epsilon$  and  $\kappa$ . In the present work, the solute is described by a set of point charges located at atomic sites, although in principle a more sophisticated description (such as the protein dipoles/Langevin dipoles of Warshel and co-workers,<sup>21,24,25</sup> a polarizable force field,<sup>26</sup> or a quantum-mechanical charge distribution) could be used to describe the solute. A “solute cavity,” constructed from atom-centered spheres, will represent the interface between these two regions. Because we employ an atomistic description of the matter inside the cavity, we set  $\epsilon = 1$  in this region.

An analytical solution of the LPBE [Eq. (1.1)] is available in the case of disjoint spherical cavities with no escaped charge.<sup>27</sup> (This analytical solution forms the basis of a new semi-analytical model for arbitrary cavity shapes.<sup>14</sup>) More often, however, the LPBE or its nonlinear precursor has been solved numerically,<sup>28–36</sup> but unfortunately these numerical

<sup>a)</sup>Electronic mail: herbert@chemistry.ohio-state.edu.

approaches are vulnerable to discontinuities in the forces that are required for molecular dynamics simulations. As such, these numerical approaches are typically used in conjunction with a frozen internal geometry for the solute molecule(s). Although some progress has been made toward reducing the magnitude of the discontinuities, in order to provide energy-conserving forces,<sup>37</sup> it is worth exploring alternative numerical methods that are specifically constructed so that the energy and its gradients are smooth functions of the nuclear coordinates of the solute molecule(s) and which are therefore immediately suitable for molecular dynamics applications. Such methods are introduced here.

Specifically, we consider a family of boundary-element approaches that is known in the quantum chemistry literature as either “apparent surface charge” models, “reaction-field” models, or (most often) “polarizable continuum” models (PCMs).<sup>17</sup> These models are easily incorporated into self-consistent field procedures and are widely used in quantum chemistry. A variety of different PCMs are available, including the conductor-like screening model (COSMO),<sup>38</sup> a slightly-modified variant known as generalized COSMO (GCOSMO),<sup>39,40</sup> which has also been called the conductor-like PCM (C-PCM),<sup>41</sup> the “integral equation formalism” (IEF-PCM);<sup>42–46</sup> and the “surface and simulation of volume polarization for electrostatics” [SS(V)PE] method.<sup>47</sup> The latter is formally equivalent to IEF-PCM at the level of integral equations,<sup>48</sup> although some differences exist, relative to IEF-PCM, in how SS(V)PE has typically been implemented numerically.<sup>49–51</sup>

For  $\mathcal{J} = 0$ , and provided that none of the solute’s charge distribution “escapes” beyond the cavity that defines the solute/continuum interface, the IEF-PCM/SS(V)PE method affords the same electrostatic solvation energy as Poisson’s equation, up to discretization errors.<sup>23</sup> Furthermore, we have recently shown how numerical IEF-PCM/SS(V)PE calculations can be performed in a manner that provides a continuous potential energy surface for the solute and also avoids spurious numerical fluctuations due to close approach of surface discretization points.<sup>50,52</sup> These properties make the IEF-PCM/SS(V)PE approach attractive for problems where forces are required.

As compared to IEF-PCM/SS(V)PE, the GCOSMO/C-PCM method is approximate but is formally and computationally simpler. Moreover, these methods are identical in the limit  $\epsilon \rightarrow \infty$ .<sup>49,51</sup> In the absence of escaped charge, GCOSMO solvation energies are essentially identical to IEF-PCM results for  $\epsilon \gtrsim 10$ .<sup>51</sup>

In this work, we are concerned with electrolyte solutions rather than neat liquid solvents. The IEF-PCM/SS(V)PE method has been adapted for solution of the LPBE rather than Poisson’s equation,<sup>23,42,43</sup> and we will refer to these adaptations as “screened PCMs” because they involve a screened Coulomb operator (Yukawa potential),  $e^{-\kappa r}/r$ . To the best of our knowledge, no analytic implementation of the screened IEF-PCM or SS(V)PE models has yet been reported. Rather, numerical quadrature has been used to evaluate integrals involving the screened Coulomb potential,<sup>23,42,43</sup> which is non-trivial because the integrand is singular when these integrals involve a single surface element. (This is actually a problem

in many different finite-element solvation models.<sup>9</sup>) In the present work, we show that our recently-developed switching/Gaussian (SWIG) approach<sup>50,52</sup> to smooth surface integration has an additional advantage in the context of screened PCMs, in that it leads to analytic expressions for the matrix elements required in these models. These expressions greatly simplify the computations and facilitate the development of analytic gradient expressions.

While the generalization of IEF-PCM/SS(V)PE to electrolyte solutions (within the Debye-Hückel limit) has been known for some time,<sup>23,42,43</sup> no analogous generalization of the conductor-like models has been reported. The reason for this is unclear to us, but we suspect that it may be due to the *ad hoc* nature of traditional derivation of COSMO, which can obscure the underlying physics of the model. In this work, we present an alternative derivation for COSMO that we think is more intuitive and which immediately suggests a screened variant of this model. Because this new model extends the “conductor-like screening model” (COSMO) to electrolytes in the Debye-Hückel limit, we refer to it as the Debye-Hückel-like screening model (DESMO).

The remainder of this work is organized as follows. Section II presents a review of the relevant PCM theory, followed by a derivation of DESMO and mathematical comparison to screened IEF-PCM/SS(V)PE. Section III provides the details of the SWIG implementation of these models. In Sec. IV, we present several numerical tests on molecular mechanics (MM) solutes, for which there is no escaped charge, in order to evaluate the accuracy of DESMO as well as our analytic implementation of screened IEF-PCM/SS(V)PE. Finally, Sec. V presents a summary.

## II. THEORY

### A. The Debye-Hückel model problem

Debye-Hückel theory<sup>53,54</sup> is developed by considering the electrostatics of a fixed spherical ion immersed in a continuum dielectric solvent, within which mobile ions of a dissociated salt are present (see Fig. 1). The positions of the mobile ions are governed by Boltzmann statistics at a specified temperature and, in combination with the dielectric medium, give rise to an average screened Coulomb potential that interacts with the fixed ion, i.e., a screened reaction-field potential. The solvent is thus characterized by a dielectric constant,  $\epsilon$ , and a Debye length  $\lambda = \kappa^{-1}$ .

For later use, let us review the analytical solution to the LPBE [Eq. (1.1)] for a single point charge,  $q$ , centered in a spherical cavity of radius  $b$  (Fig. 1). The mobile ions are assumed to be hard spheres of radius  $c$  that form a layer of width  $c$  around the solute cavity. Mobile ions cannot penetrate into this layer, which is therefore known as the *ion exclusion layer* (IEL). Let  $a = b + c$  be the distance from the cavity-centered point charge to the bulk solvent boundary. The interior of the cavity ( $r < b$ ) is assumed to have a dielectric constant of unity, whereas the IEL and bulk solvent have dielectric constant  $\epsilon$ . Under these assumptions, Eq. (1.1) can be solved exactly for all space.<sup>53–55</sup> With the point charge  $q$  located at the

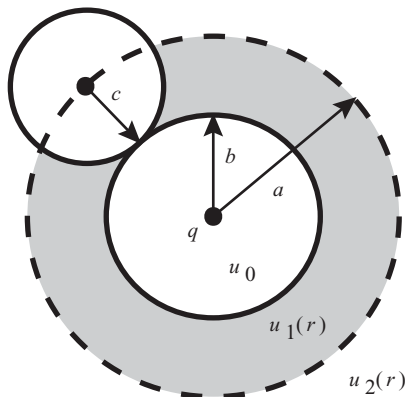


FIG. 1. Schematic representation of the spherical Debye-Hückel model system. The point charge  $q$  is contained within a sphere of radius  $b$ , and the shaded region represents the ion exclusion layer.

origin, the solution is

$$U(r) = \begin{cases} u_0 & \text{for } 0 < r < b \\ u_1(r) & \text{for } b < r < a \\ u_2(r) & \text{for } r > a \end{cases}, \quad (2.1)$$

where

$$u_0 = \frac{q[1 + \kappa(a - b)]}{\epsilon b(1 + \kappa a)} \quad (2.2a)$$

$$u_1(r) = \frac{q[1 + \kappa(a - r)]}{\epsilon r(1 + \kappa a)} \quad (2.2b)$$

$$u_2(r) = \frac{q e^{\kappa(a-r)}}{\epsilon r(1 + \kappa a)}. \quad (2.2c)$$

For the region  $r > a$ , note in particular the presence of the screened Coulomb potential,  $e^{-\kappa r}/r$ , and the factor

$$\gamma = \frac{e^{\kappa a}}{1 + \kappa a}, \quad (2.3)$$

in Eq. (2.2c). The factor  $\gamma$  alone accounts for the finite radius of the ions, and we therefore refer to  $\gamma$  as the *IEL factor*. The total electrostatic energy of the Debye-Hückel model system is<sup>55,56</sup>

$$W = -\frac{q^2}{2b} \left[ 1 - \frac{1}{\epsilon} + \frac{\kappa b}{\epsilon(1 + \kappa a)} \right]. \quad (2.4)$$

For  $\kappa = 0$ , this expression reduces to the Born ion model.<sup>57</sup>

In the remainder of this work, we assume that  $c = 0$  (i.e., that the mobile solvent ions are point charges) so that the IEL coincides with the solute cavity. (The IEL still functions to prevent mobile solvent ions from penetrating the solute cavity interior.) This assumption is tacitly adopted in the derivations of the screened IEF-PCM and screened SS(V)PE models as well.<sup>23</sup> The simplification that this assumption provides, in the context of PCMs, is that only one surface is present.

## B. Boundary conditions and integral operators

Next, let us establish some notation and also briefly review the boundary conditions and relevant integral operators that appear in various PCMs. We use the notation in Ref. 23 as much as possible. For more details on the integrals operators, see Refs. 23 and 46.

The total electrostatic potential,  $U(\vec{r})$ , of the solute/solvent system can be separated into two parts,

$$U(\vec{r}) = \phi_0^p(\vec{r}) + U^{\text{rxn}}(\vec{r}), \quad (2.5)$$

where  $\phi_0^p(\vec{r})$  is the vacuum electrostatic potential produced by the solute's charge density,  $\rho(\vec{r})$ , and  $U^{\text{rxn}}(\vec{r})$  is the reaction-field potential generated by the continuum, in response to  $\rho(\vec{r})$ . The solute is enclosed by a surface,  $\Gamma$ , that constitutes a boundary between the interior volume,  $V^{\text{int}}$  (where the dielectric constant is unity), and the exterior volume,  $V^{\text{ext}}$ , which is characterized by a dielectric constant,  $\epsilon$ , and an inverse Debye length,  $\kappa$ . Points constrained to lie on  $\Gamma$  are denoted by  $\vec{s}$ , whereas  $\vec{r}$  can range over all space.

The total electrostatic potential is continuous across  $\Gamma$ . If  $\vec{s}^{\text{int}}$  and  $\vec{s}^{\text{ext}}$  represent points that reside on the interior and exterior faces of  $\Gamma$ , respectively, then

$$U(\vec{s}^{\text{int}}) = U(\vec{s}^{\text{ext}}). \quad (2.6)$$

Given Eq. (2.5), this also implies that the reaction-field potential must be continuous across  $\Gamma$ :

$$U^{\text{rxn}}(\vec{s}^{\text{int}}) = U^{\text{rxn}}(\vec{s}^{\text{ext}}). \quad (2.7)$$

The gradient of  $U$ , on the other hand, is subject to a “jump” boundary condition. Specifically, the outward-pointing normal electric field generated by  $U$  is discontinuous across  $\Gamma$ :

$$\partial_{\vec{s}} U(\vec{s}^{\text{int}}) = \epsilon \partial_{\vec{s}} U(\vec{s}^{\text{ext}}). \quad (2.8)$$

We use the symbol  $\partial_{\vec{s}}$  as an abbreviation for the outward-pointing normal derivative,  $\partial/\partial \vec{n}_{\vec{s}}$ . Because  $\partial_{\vec{s}} \phi_0^p(\vec{r})$  is continuous across  $\Gamma$ , the reaction field is solely responsible for the jump boundary condition,<sup>49</sup> and we have

$$\partial_{\vec{s}} U^{\text{rxn}}(\vec{s}^{\text{ext}}) = -\left(\frac{\epsilon - 1}{\epsilon}\right) \partial_{\vec{s}} \phi_0^p(\vec{s}) + \frac{1}{\epsilon} \partial_{\vec{s}} U^{\text{rxn}}(\vec{s}^{\text{int}}). \quad (2.9)$$

The screened electrostatic potential produced by a solute charge density  $\rho$  is

$$\phi_{\kappa}^p(\vec{r}) = \int \rho(\vec{r}') \frac{e^{-\kappa|\vec{r}-\vec{r}'|}}{|\vec{r}-\vec{r}'|} d^3\vec{r}'. \quad (2.10)$$

Similarly, the screened electrostatic potential produced by a single-layer surface charge density,  $\sigma(\vec{s})$ , is

$$\chi_{\kappa}^{\sigma}(\vec{r}) = \int \sigma(\vec{s}) \frac{e^{-\kappa|\vec{r}-\vec{s}|}}{|\vec{r}-\vec{s}|} d^2\vec{s}. \quad (2.11)$$

In the limit  $\kappa \rightarrow 0$ , these potentials reduce to the corresponding unscreened (vacuum) electrostatic potentials.

The self-adjoint integral operator  $\hat{S}_{\kappa}$  is defined such that the action of  $\hat{S}_{\kappa}$  on  $\sigma(\vec{s})$  produces the screened potential at the surface point  $\vec{s}$ :

$$\hat{S}_{\kappa} \sigma(\vec{s}) = \chi_{\kappa}^{\sigma}(\vec{s}). \quad (2.12)$$

Note that  $\chi_\kappa^\sigma(\vec{s})$ , therefore, depends on the surface charge across all of  $\Gamma$ . The quantity  $\partial_{\vec{s}} \chi_\kappa^\sigma(\vec{s})$  represents the negative normal component of the screened electric field produced by  $\sigma(\vec{s})$ , evaluated at the point  $\vec{s}$ . The integral operator  $\hat{D}_\kappa^\dagger$  is defined such that it generates this screened negative normal electric field, according to

$$\hat{D}_\kappa^\dagger \sigma(\vec{s}) = \partial_{\vec{s}} \chi_\kappa^\sigma(\vec{s}). \quad (2.13)$$

The discontinuity inherent in the jump boundary condition can then be expressed as<sup>23</sup>

$$[\hat{D}_\kappa^\dagger + 2\pi\hat{\mathcal{I}}] \sigma(\vec{s}) = \partial_{\vec{s}} \chi_\kappa^\sigma(\vec{s}^{\text{int}}), \quad (2.14a)$$

$$[\hat{D}_\kappa^\dagger - 2\pi\hat{\mathcal{I}}] \sigma(\vec{s}) = \partial_{\vec{s}} \chi_\kappa^\sigma(\vec{s}^{\text{ext}}). \quad (2.14b)$$

The adjoint of  $\hat{D}_\kappa^\dagger$  is  $\hat{D}_\kappa$ , and these operators obey the relation  $\hat{D}_\kappa \hat{S}_\kappa = \hat{S}_\kappa \hat{D}_\kappa^\dagger$ . Similar to the electrostatic potentials, these integral operators reduce to their unscreened forms in the limit that  $\kappa \rightarrow 0$ .

The total energy of the solute/solvent supersystem is

$$W = E_0 + E_{\text{pol}}, \quad (2.15)$$

where  $E_0$  is the energy of  $\rho(\vec{r})$  in vacuum. The second term,  $E_{\text{pol}}$ , is the *reaction field energy* (also known as the *electrostatic solvation energy*) that arises from polarization of the dielectric continuum. This quantity is given by

$$E_{\text{pol}} = \frac{1}{2} \int \rho(\vec{r}) U^{\text{rxn}}(\vec{r}) d^3\vec{r}, \quad (2.16)$$

where the factor of 1/2 accounts for polarization work. As pointed out by Chipman,<sup>23</sup> all of the PCMs considered here invoke the *ansatz*

$$U^{\text{rxn}}(\vec{r}) = \chi_0^\sigma(\vec{r}), \quad (2.17)$$

for all  $\vec{r}$ .

## C. Conductor-like screening model

### 1. Traditional derivation

Conventional derivations of COSMO and the closely-related GCOSMO/C-PCM method begin by assuming that the solute resides completely inside a cavity that is embedded in a conductor.<sup>38-41</sup> This implies that  $U(\vec{r})$  vanishes at the cavity surface,  $\Gamma$ , and is zero beyond this boundary:

$$U(\vec{r}) = \begin{cases} \phi_0^\rho(\vec{r}) + \chi_0^\sigma(\vec{r}) & \text{for } \vec{r} \in V^{\text{int}} \\ 0 & \text{for } \vec{r} \in V^{\text{ext}} \end{cases}. \quad (2.18)$$

To ensure that the electrostatic potential is continuous across the cavity surface [Eq. (2.6)], one must then have

$$\hat{S}_0 \sigma^{\text{conductor}}(\vec{s}) = -\phi_0^\rho(\vec{s}). \quad (2.19)$$

To obtain a model that works for a continuum with a finite dielectric constant, rather than a conductor, the standard approach is to scale  $\sigma^{\text{conductor}}(\vec{s})$  by an *ad hoc* factor,  $f_\varepsilon$ . The equation to be solved is then

$$\hat{S}_0 \sigma^{\text{COSMO}}(\vec{s}) = -f_\varepsilon \phi_0^\rho(\vec{s}). \quad (2.20)$$

In the original derivation of COSMO,<sup>38</sup> Klamt and Schüürman propose the scaling factor  $f_\varepsilon = (\varepsilon - 1)/(\varepsilon + 0.5)$ . The GCOSMO/C-PCM method also uses Eq. (2.20) but with  $f_\varepsilon = (\varepsilon - 1)/\varepsilon$ . As compared to the original COSMO, the latter choice more closely approximates Gauss' Law for the surface charge density.<sup>39,40</sup>

### 2. Alternative derivation

The difficulty with this derivation, in the context of electrolyte solutions, is that the scaling factor  $f_\varepsilon$  is applicable only for  $\kappa = 0$ . For  $\kappa > 0$ , no analogous scaling factor exists for arbitrary cavity shapes. As such, the derivation of COSMO presented above cannot be extended to electrolytic solvents. Here, we reconsider the derivation of COSMO.

Rather than starting from the conductor limit and later scaling the surface charge, one can derive COSMO starting from an *ansatz* that actually resembles a cavity immersed in a dielectric [cf. Eq. (2.18)]:

$$U(\vec{r}) = \begin{cases} \phi_0^\rho(\vec{r}) + \chi_0^\sigma(\vec{r}) & \text{for } \vec{r} \in V^{\text{int}} \\ \phi_0^\rho(\vec{r})/\varepsilon & \text{for } \vec{r} \in V^{\text{ext}} \end{cases}. \quad (2.21)$$

Enforcing the continuity condition [Eq. (2.6)] upon this *ansatz* immediately affords Eq. (2.20), with  $f_\varepsilon = (\varepsilon - 1)/\varepsilon$  as in GCOSMO/C-PCM. At no point do we appeal to the conductor limit. In view of this result, the solution of Eq. (2.20) can be interpreted as that particular surface charge density,  $\sigma^{\text{COSMO}}(\vec{s})$ , that makes  $U(\vec{r}) = \phi_0^\rho(\vec{r})/\varepsilon$  for all points  $\vec{r} \in V^{\text{ext}}$ . This interpretation is not obvious from the conventional derivation of COSMO.

Although the surface charge density  $\sigma^{\text{COSMO}}(\vec{s})$  that is obtained from Eq. (2.21) satisfies the continuity condition, it does not exactly satisfy the jump boundary condition except in special cases. This is immediately clear from the normal derivative of  $U^{\text{rxn}}(\vec{s}^{\text{ext}})$ , within the *ansatz* of Eq. (2.21):

$$\partial_{\vec{s}} U^{\text{rxn}}(\vec{s}^{\text{ext}}) = -\left(\frac{\varepsilon - 1}{\varepsilon}\right) \partial_{\vec{s}} \phi_0^\rho(\vec{s}). \quad (2.22)$$

This is *not* the correct jump boundary condition, as it lacks the term  $\varepsilon^{-1} \partial_{\vec{s}} U^{\text{rxn}}(\vec{s}^{\text{int}})$  that appears in Eq. (2.9). The GCOSMO/C-PCM method only approximately satisfies the jump boundary condition, and Eq. (2.22) should be regarded as the fundamental approximation in this model. On the other hand, the missing term is proportional to  $\varepsilon^{-1}$ , so Eq. (2.22) is exact in the conductor limit,  $\varepsilon \rightarrow \infty$ . It is also exact if  $\partial_{\vec{s}} U^{\text{rxn}}(\vec{s}^{\text{int}}) = 0$ , in which case  $U^{\text{rxn}}(\vec{s}^{\text{int}})$  is constant. Examples where the latter situation is realized include the trivial case of  $\varepsilon = 1$  (i.e., the gas phase), where  $U^{\text{rxn}}(\vec{s}^{\text{int}}) \equiv 0$ , or for certain highly symmetrical systems, such as a uniform surface charge distribution over a spherical cavity, as in the Born ion model.

Equation (2.22) suggests an equivalent, auxiliary equation that could be solved to obtain  $\sigma^{\text{COSMO}}(\vec{s})$ . Using Eq. (2.22) in conjunction with Eq. (2.14b), one obtains

$$(\hat{D}_0^\dagger - 2\pi\hat{\mathcal{I}}) \sigma^{\text{COSMO}}(\vec{s}) = -\left(\frac{\varepsilon - 1}{\varepsilon}\right) \partial_{\vec{s}} \phi_0^\rho(\vec{s}). \quad (2.23)$$

To illustrate that this equation is equivalent to Eq. (2.20), we operate on Eq. (2.23) with  $\hat{S}_0$  and then use the identity  $\hat{D}_0 \hat{S}_0 = \hat{S}_0 \hat{D}_0^\dagger$  to arrive at

$$(\hat{D}_0 - 2\pi\hat{\mathcal{I}})\hat{S}_0\sigma^{\text{COSMO}}(\vec{s}) = -\left(\frac{\varepsilon - 1}{\varepsilon}\right)\hat{S}_0\partial_{\vec{s}}\phi_0^\rho(\vec{s}). \quad (2.24)$$

Next, we can make use of an identity derived by Chipman,<sup>23</sup>

$$-(\hat{D}_\kappa - 2\pi\hat{\mathcal{I}})\phi_\kappa^\rho(\vec{s}) + \hat{S}_\kappa\partial_{\vec{s}}\phi_\kappa^\rho(\vec{s}) = 4\pi\phi_\kappa^\rho(\vec{s}), \quad (2.25)$$

where  $\phi_\kappa^\rho(\vec{s})$  is the screened electrostatic potential due to that portion of solute's charge density,  $\rho(\vec{r})$ , that penetrates beyond the solute cavity. For the salt-free case ( $\kappa = 0$ ), and when solute charge density is completely contained inside the cavity [ $\phi_\kappa^\rho(\vec{s}) \equiv 0$ ], Eq. (2.25) can be substituted into Eq. (2.24) to obtain Eq. (2.20). Indeed, we have confirmed in numerical tests that the ASC,  $\sigma^{\text{COSMO}}(\vec{s})$ , that is obtained from Eq. (2.23) is equivalent to that obtained from solution of Eq. (2.20). However, Eq. (2.20) is much easier to solve in practice because it does not involve surface normal derivatives.

#### D. Debye-Hückel-like screening model

Following the logic of our alternative derivation of GCOSMO/C-PCM, it is now clear how electrolytic screening effects can be incorporated within this model. We choose an *ansatz* for  $U(\vec{r})$  such that any point outside the cavity has a screened potential [cf. Eq. (2.21)]:

$$U(\vec{r}) = \begin{cases} \phi_0^\rho(\vec{r}) + \chi_0^\sigma(\vec{r}) & \text{for } \vec{r} \in V^{\text{int}} \\ \phi_\kappa^\rho(\vec{r})/\varepsilon & \text{for } \vec{r} \in V^{\text{ext}} \end{cases}. \quad (2.26)$$

Applying the continuity condition to this *ansatz* leads immediately to an equation for the surface charge,

$$\hat{S}_0\sigma^{\text{DESMO}}(\vec{s}) = \frac{1}{\varepsilon}\phi_\kappa^\rho(\vec{s}) - \phi_0^\rho(\vec{s}). \quad (2.27)$$

Equation (2.27) is the primary equation for our Debye-Hückel-like screening model. This model involves the same integral operator,  $\hat{S}_0$ , that is used in COSMO and therefore retains a great deal of COSMO's simplicity, relative to the screened versions of SS(V)PE and IEF-PCM. In the limit  $\kappa \rightarrow 0$ , Eq. (2.27) reduces to the GCOSMO/C-PCM equation, as expected.

Similar to GCOSMO/C-PCM, DESMO only approximately satisfies the jump boundary condition [Eq. (2.9)]. Starting from Eq. (2.25) with  $\phi_\kappa^\rho(\vec{s}) = 0$ , and substituting Eq. (2.27), we arrive at a secondary equation for  $\sigma^{\text{DESMO}}(\vec{s})$ :

$$\begin{aligned} & \left(\hat{\mathcal{I}} - \frac{1}{2\pi}\hat{D}_\kappa\right)\hat{S}_0\sigma^{\text{DESMO}}(\vec{s}) \\ &= -\left(\hat{\mathcal{I}} - \frac{1}{2\pi}\hat{D}_\kappa\right)\phi_0^\rho(\vec{s}) - \frac{1}{2\pi\varepsilon}\hat{S}_\kappa\partial_{\vec{s}}\phi_0^\rho(\vec{s}). \end{aligned} \quad (2.28)$$

At this point, Eq. (2.28) is not a completely transparent result, but its importance will become apparent below.

#### E. Screened SS(V)PE and screened IEF-PCM

It is useful to summarize Chipman's derivation of the screened SS(V)PE model,<sup>23</sup> for comparison to DESMO. This derivation begins by invoking a pair of separate surface charge distributions,  $\sigma^{\text{int}}$  and  $\sigma^{\text{ext}}$ , which reside on the interior and exterior faces of  $\Gamma$ , respectively. The total electrostatic potential within this *ansatz* is

$$U(\vec{r}) = \begin{cases} \phi_0^\rho(\vec{r}) + \chi_0^{\sigma^{\text{int}}}(\vec{r}) & \text{for } \vec{r} \in V^{\text{int}} \\ [\phi_\kappa^\rho(\vec{r}) + \chi_\kappa^{\sigma^{\text{ext}}}(\vec{r})]/\varepsilon & \text{for } \vec{r} \in V^{\text{ext}} \end{cases}. \quad (2.29)$$

The continuity condition for this *ansatz* takes the form

$$\hat{S}_0\sigma^{\text{int}}(\vec{s}) - \frac{1}{\varepsilon}\hat{S}_\kappa\sigma^{\text{ext}}(\vec{s}) = \frac{1}{\varepsilon}\phi_\kappa^\rho(\vec{s}) - \phi_0^\rho(\vec{s}), \quad (2.30)$$

whereas the jump boundary condition is

$$\begin{aligned} & \left(\hat{\mathcal{I}} + \frac{1}{2\pi}\hat{D}_0^\dagger\right)\sigma^{\text{int}}(\vec{s}) + \left(\hat{\mathcal{I}} - \frac{1}{2\pi}\hat{D}_\kappa^\dagger\right)\sigma^{\text{ext}}(\vec{s}) \\ &= \frac{1}{2\pi}[\partial_{\vec{s}}\phi_\kappa^\rho(\vec{s}) - \partial_{\vec{s}}\phi_0^\rho(\vec{s})]. \end{aligned} \quad (2.31)$$

As written, Eqs. (2.30) and (2.31) are coupled, but they can be manipulated so as to uncouple  $\sigma^{\text{int}}$  and  $\sigma^{\text{ext}}$ . The result is the primary equation for screened SS(V)PE,<sup>23</sup>

$$\begin{aligned} & \left[\left(\hat{\mathcal{I}} - \frac{1}{2\pi}\hat{D}_\kappa\right)\hat{S}_0 + \frac{1}{\varepsilon}\hat{S}_\kappa\left(\hat{\mathcal{I}} + \frac{1}{2\pi}\hat{D}_0^\dagger\right)\right]\sigma^{\text{int}}(\vec{s}) \\ &= \left(\hat{\mathcal{I}} - \frac{1}{2\pi}\hat{D}_\kappa\right)\left[\frac{1}{\varepsilon}\phi_\kappa^\rho(\vec{s}) - \phi_0^\rho(\vec{s})\right] \\ &+ \frac{1}{2\pi\varepsilon}\hat{S}_\kappa[\partial_{\vec{s}}\phi_\kappa^\rho(\vec{s}) - \partial_{\vec{s}}\phi_0^\rho(\vec{s})]. \end{aligned} \quad (2.32)$$

Chipman then sets  $\sigma^{\text{int}}(\vec{s}) = \sigma^{\text{SS(V)PE}}(\vec{s})$ , which is used in Eq. (2.17) to obtain the reaction-field potential  $U^{\text{rxn}}(\vec{r})$  that is used to evaluate  $E_{\text{pol}}$ .

The screened IEF-PCM method is derived using a somewhat similar approach,<sup>43</sup> considering interior and exterior faces of  $\Gamma$ , but using only a single surface charge distribution,  $\sigma^{\text{IEF-PCM}}(\vec{s})$ . The resulting screened IEF-PCM equation is<sup>43,46</sup>

$$\begin{aligned} & \left[\left(\hat{\mathcal{I}} - \frac{1}{2\pi}\hat{D}_\kappa\right)\hat{S}_0 + \frac{1}{\varepsilon}\hat{S}_\kappa\left(\hat{\mathcal{I}} + \frac{1}{2\pi}\hat{D}_0^\dagger\right)\right]\sigma^{\text{IEF-PCM}}(\vec{s}) \\ &= -\left(\hat{\mathcal{I}} - \frac{1}{2\pi}\hat{D}_\kappa\right)\phi_0^\rho(\vec{s}) - \frac{1}{2\pi\varepsilon}\hat{S}_\kappa\partial_{\vec{s}}\phi_0^\rho(\vec{s}). \end{aligned} \quad (2.33)$$

The identity in Eq. (2.25) can be rearranged to yield

$$\left(\hat{\mathcal{I}} - \frac{1}{2\pi}\hat{D}_\kappa\right)\phi_\kappa^\rho(\vec{s}) + \frac{1}{2\pi}\hat{S}_\kappa\partial_{\vec{s}}\phi_\kappa^\rho(\vec{s}) = 2\phi_\kappa^\rho(\vec{s}). \quad (2.34)$$

Then, as noted in Ref. 23, Eq. (2.34) can be used to recast the right side of Eq. (2.32) into a form analogous to that of Eq. (2.33). Following this manipulation, the basic equation

for screened SS(V)PE [Eq. (2.32)] can be written as

$$\begin{aligned} & \left[ \left( \hat{\mathcal{I}} - \frac{1}{2\pi} \hat{\mathcal{D}}_\kappa \right) \hat{\mathcal{S}}_0 + \frac{1}{\varepsilon} \hat{\mathcal{S}}_\kappa \left( \hat{\mathcal{I}} + \frac{1}{2\pi} \hat{\mathcal{D}}_0^\dagger \right) \right] \sigma^{\text{SS(V)PE}}(\vec{s}) \\ & = - \left( \hat{\mathcal{I}} - \frac{1}{2\pi} \hat{\mathcal{D}}_\kappa \right) \phi_0^\rho(\vec{s}) - \frac{1}{2\pi\varepsilon} \hat{\mathcal{S}}_\kappa \partial_{\vec{s}} \phi_0^\rho(\vec{s}) + \frac{2}{\varepsilon} \phi_\kappa^\rho(\vec{s}). \end{aligned} \quad (2.35)$$

Comparing this to Eq. (2.33), it is apparent that the screened versions of SS(V)PE and IEF-PCM are identical except for the term involving  $\phi_\kappa^\rho(\vec{s})$ , which is absent in the latter. As such, these two models are equivalent in the absence of escaped charge. The two methods also become equivalent in the limit  $\varepsilon \rightarrow \infty$ .

Let us now compare DESMO to screened SS(V)PE and IEF-PCM, continuing the discussion left off at the end of Sec. II D. The secondary form of the DESMO equation, Eq. (2.28), is remarkably similar to Eq. (2.33) but it lacks the second term in square brackets in Eq. (2.33). However, this missing term is proportional to  $\varepsilon^{-1}$ , and Eq. (2.28) becomes exact in the limit  $\varepsilon \rightarrow \infty$ . DESMO is also exact if

$$\left( \hat{\mathcal{I}} + \frac{1}{2\pi} \hat{\mathcal{D}}_0^\dagger \right) \sigma^{\text{DESMO}}(\vec{s}) = \frac{1}{2\pi} [\partial_{\vec{s}} \phi_\kappa^\rho(\vec{s}) - \partial_{\vec{s}} \phi_0^\rho(\vec{s})], \quad (2.36)$$

which can be seen by substituting Eq. (2.36) into Eq. (2.32). The left side of Eq. (2.36) is simply  $\partial_{\vec{s}} \chi_\kappa^\sigma(\vec{s}^{\text{int}})$  scaled by a factor of  $2\pi$ , and it expresses the screened version of the limit in which GCOSMO/C-PCM is exact,  $\partial_{\vec{s}} U^{\text{rxn}}(\vec{s}^{\text{int}}) = 0$ . Clearly, Eq. (2.36) reduces to the condition  $\partial_{\vec{s}} \chi_\kappa^\sigma(\vec{s}^{\text{int}}) = 0$  [*i.e.*  $\partial_{\vec{s}} U^{\text{rxn}}(\vec{s}^{\text{int}}) = 0$ ] when  $\kappa = 0$ .

### III. DISCRETIZATION

In this section, we discretize the integral equations that define the DESMO, screened SS(V)PE, and screened IEF-PCM methods, to obtain finite-dimensional matrix equations. This discretization is accomplished using the SWIG procedure that we have recently introduced for the *unscreened* SS(V)PE/IEF-PCM and GCOSMO/C-PCM methods.<sup>50–52</sup> Complete details of the SWIG procedure can be found in Ref. 50; the essential aspects are summarized here.

#### A. Overview of the SWIG approach

The solute cavity surface is constructed from a union of atom-centered spheres whose radii are parameters of the model. Although this approach has occasionally been criticized,<sup>58,59</sup> and more sophisticated approaches have been explored,<sup>60–63</sup> the use of parameterized atomic radii remains ubiquitous in the PCM literature and provides a simple definition for the cavity surface that will facilitate comparison with exact results.

Lebedev grids<sup>64</sup> are used to discretize the surface of each sphere into a finite set of points,  $\{\vec{s}_i\}$ . Each grid point is associated with a surface area  $\tilde{a}_i = w_i R_I^2$ , where  $R_I$  is the radius of the atomic sphere on which the point  $\vec{s}_i$  resides, and  $w_i$  is the Lebedev quadrature weight associated with this grid point.

A straightforward way to discretize the integral equations in Sec. II would be to place a point charge,  $q_i$ , at each grid point  $\vec{s}_i$ , thus replacing  $\sigma(\vec{s})$  with a vector of point charges,  $\mathbf{q}$ .

The problem with such an approach is that surface grid points may emerge from—or vanish into—the interior of the cavity as the nuclei move, leading to discontinuities in the potential energy surface. To avoid these, we introduce a switching function,  $F_i$ , that smoothly attenuates  $\vec{s}_i$ 's contribution to the PCM equations, as the point  $\vec{s}_i$  passes through a buffer region surrounding the cavity surface. (Precisely how  $F_i$  is incorporated into the matrix elements is discussed in Sec. III C.) Insofar as  $F_i$  is a smooth function of the nuclear coordinates, this guarantees a smooth potential energy surface. Note also that the surface area associated with  $\vec{s}_i$  is<sup>52</sup>

$$a_i = \tilde{a}_i F_i = w_i F_i R_I^2. \quad (3.1)$$

We have observed that potential energy surfaces that are rigorously smooth (in the mathematical sense of possessing continuous derivatives) may still suffer from spurious oscillations in the energy or gradient, which arise due to the singular nature of the Coulomb potential between the surface point charges.<sup>50–52</sup> Introduction of a switching function actually exacerbates this problem, as it allows grid points to approach one another more closely than would be the case if we simply discarded all interior grid points. This problem can be overcome via “Gaussian blurring” of the point charges  $q_i$ .<sup>50,52,65</sup> To wit, we introduce a set of spherical Gaussian functions,  $\{g_i\}$ , that are centered at the points  $\vec{s}_i$ :

$$g_i(\vec{r}) = q_i \left( \frac{\zeta_i}{\pi} \right)^{3/2} e^{-\zeta_i^2 |\vec{r} - \vec{s}_i|^2}. \quad (3.2)$$

The exponent  $\zeta_i$ , which controls the width of  $g_i$ , depends upon the number of Lebedev grid points used to discretize the spheres. Values of  $\zeta_i$  were taken from Ref. 66, where they were optimized to obtain accurate solvation energies for the Born ion model across a range of dielectric constants. The Coulomb interaction between  $g_i(\vec{r})$  and  $g_j(\vec{r})$  is finite even as  $|\vec{s}_i - \vec{s}_j| \rightarrow 0$  and in our experience this is sufficient to remove spurious fluctuations in the energy and gradient.<sup>50–52</sup>

#### B. Electrostatic solvation energy and gradient

Upon discretization, the electrostatic potential  $\phi_\kappa^\rho$  and the normal electric field  $\partial_{\vec{s}} \phi_\kappa^\rho$  are replaced by vectors  $\mathbf{v}_\kappa$  and  $\mathbf{v}_\kappa^\perp$ , respectively, whose elements are

$$v_{\kappa,i} = \phi_\kappa^\rho(\vec{s}_i), \quad (3.3a)$$

$$v_{\kappa,i}^\perp = \partial_{\vec{s}} \phi_\kappa^\rho(\vec{s}_i). \quad (3.3b)$$

Note that the unscreened electrostatic potential,  $\mathbf{v}_0$ , can be viewed as a special case of  $\mathbf{v}_\kappa$ . The point charges  $q_i$  are collected in a vector  $\mathbf{q}$  that, together with the surface areas  $a_i$ , represent the discretization of  $\sigma(\vec{s})$ .

For consistency with the general PCM framework,<sup>49,50</sup> we wish to cast the integral equations of Sec. II into finite-dimensional matrix equations of the form

$$\mathbf{K}\mathbf{q} = \mathbf{R}\mathbf{v}_0, \quad (3.4)$$

TABLE I. Definitions of  $\mathbf{K}$  and  $\mathbf{R}$  for screened PCMs.

Method	Matrix $\mathbf{K}$	Matrix $\mathbf{R}$
DESMO	$\mathbf{S}_0$	$-(\mathbf{I} - \frac{1}{\epsilon}\mathbf{M})$
IEF-PCM	$(\mathbf{I} - \frac{1}{2\pi}\mathbf{D}_\kappa\mathbf{A})\mathbf{S}_0 + \frac{1}{\epsilon}\mathbf{S}_\kappa(\mathbf{I} + \frac{1}{2\pi}\mathbf{A}\mathbf{D}_0^\dagger)$	$(\mathbf{I} - \frac{1}{2\pi}\mathbf{D}_\kappa\mathbf{A}) - \frac{1}{2\pi\epsilon}\mathbf{S}'_\kappa\mathbf{L}$
SS(V)PE	$(\mathbf{I} - \frac{1}{2\pi}\mathbf{D}_\kappa\mathbf{A})\mathbf{S}_0 + \frac{1}{\epsilon}\mathbf{S}_\kappa(\mathbf{I} + \frac{1}{2\pi}\mathbf{A}\mathbf{D}_0^\dagger)$	$(\mathbf{I} - \frac{1}{2\pi}\mathbf{D}_\kappa\mathbf{A})(\frac{1}{\epsilon}\mathbf{M} - \mathbf{I}) + \frac{1}{2\pi\epsilon}\mathbf{S}'_\kappa(\mathbf{N} - \mathbf{L})$

whose formal solution is

$$\mathbf{q} = \mathbf{Q}\mathbf{v}_0, \quad (3.5)$$

where  $\mathbf{Q} = \mathbf{K}^{-1}\mathbf{R}$  is known as the *solvent response matrix*. Table I defines the  $\mathbf{K}$  and  $\mathbf{R}$  matrices for DESMO and screened SS(V)PE in terms of  $\mathbf{S}_\kappa$  and  $\mathbf{D}_\kappa$ , which are the discretized forms of the operators  $\hat{\mathcal{S}}_\kappa$  and  $\hat{\mathcal{D}}_\kappa$  from Sec. II. In addition, we have introduced a diagonal matrix  $\mathbf{A}$  that contains the surface element areas,  $A_{ij} = a_i \delta_{ij}$ , as well as auxiliary matrices  $\mathbf{L}$ ,  $\mathbf{M}$ , and  $\mathbf{N}$ . The latter are each diagonal, with matrix elements

$$L_{ij} = \delta_{ij}v_{0,i}^\perp/v_{0,i}, \quad (3.6a)$$

$$M_{ij} = \delta_{ij}v_{\kappa,i}/v_{0,i}, \quad (3.6b)$$

$$N_{ij} = \delta_{ij}v_{\kappa,i}^\perp/v_{0,i}. \quad (3.6c)$$

Following discretization, the reaction-field energy can be written in a variety of equivalent forms:

$$E_{\text{pol}} = \frac{1}{2}\mathbf{v}_0^\dagger\mathbf{q} = \frac{1}{2}\mathbf{q}^\dagger\mathbf{Q}^{-1}\mathbf{q} = \frac{1}{2}\mathbf{v}_0^\dagger\mathbf{Q}\mathbf{v}_0. \quad (3.7)$$

Although  $\mathbf{Q}$  is generally not symmetric, it is easily shown that  $E_{\text{pol}}$  is invariant to symmetrization of  $\mathbf{Q}$ , i.e., we could replace  $\mathbf{Q}$  in Eq. (3.7) with the symmetric matrix  $\tilde{\mathbf{Q}} = (\mathbf{Q} + \mathbf{Q}^\dagger)/2$ . For solutes described using quantum mechanics (at the self-consistent field level), this symmetrization is important because if  $\mathbf{Q} = \mathbf{Q}^\dagger$ , then one can evaluate the analytic gradient of  $E_{\text{pol}}$  without solving the coupled-perturbed equations.<sup>67</sup> In practice, symmetrization of  $\mathbf{Q}$  requires solving Eq. (3.5) twice, the second time with  $\mathbf{Q}$  replaced by  $\mathbf{Q}^\dagger$ , as discussed in Ref. 50. This technique will be exploited in Sec. III E, when we introduce the DESMO analytic gradient.

TABLE II. Definitions of  $\mathbf{K}^x$  and  $\mathbf{R}^x$  for screened PCMs.

Method	Matrix $\mathbf{K}^x$	Matrix $\mathbf{R}^x$
DESMO	$\mathbf{S}_0^x$	$\frac{1}{\epsilon}\mathbf{M}^x$
IEF-PCM	$-\frac{1}{2\pi}(\mathbf{D}_\kappa^x\mathbf{A} + \mathbf{D}_\kappa\mathbf{A}^x)\mathbf{S}_0 + (\mathbf{I} - \frac{1}{2\pi}\mathbf{D}_\kappa\mathbf{A})\mathbf{S}_0^x$ $+ \frac{1}{\epsilon}\mathbf{S}_\kappa^x(\mathbf{I} + \frac{1}{2\pi}\mathbf{A}\mathbf{D}_0^\dagger) + \frac{1}{2\pi\epsilon}\mathbf{S}_\kappa[\mathbf{A}^x\mathbf{D}_0^\dagger + \mathbf{A}(\mathbf{D}_0^\dagger)^x]$	$-\frac{1}{2\pi}(\mathbf{D}_\kappa^x\mathbf{A} + \mathbf{D}_\kappa\mathbf{A}^x) - \frac{1}{2\pi\epsilon}(\mathbf{S}_\kappa^x\mathbf{L} + \mathbf{S}'_\kappa\mathbf{L}^x)$
SS(V)PE	$-\frac{1}{2\pi}(\mathbf{D}_\kappa^x\mathbf{A} + \mathbf{D}_\kappa\mathbf{A}^x)\mathbf{S}_0 + (\mathbf{I} - \frac{1}{2\pi}\mathbf{D}_\kappa\mathbf{A})\mathbf{S}_0^x$ $+ \frac{1}{\epsilon}\mathbf{S}_\kappa^x(\mathbf{I} + \frac{1}{2\pi}\mathbf{A}\mathbf{D}_0^\dagger) + \frac{1}{2\pi\epsilon}\mathbf{S}_\kappa[\mathbf{A}^x\mathbf{D}_0^\dagger + \mathbf{A}(\mathbf{D}_0^\dagger)^x]$	$-\frac{1}{2\pi}(\mathbf{D}_\kappa^x\mathbf{A} + \mathbf{D}_\kappa\mathbf{A}^x)(\frac{1}{\epsilon}\mathbf{M} - \mathbf{I}) + \frac{1}{\epsilon}(\mathbf{I} - \frac{1}{2\pi}\mathbf{D}_0\mathbf{A})\mathbf{M}^x$ $-\frac{1}{2\pi\epsilon}\mathbf{S}_\kappa^x(\mathbf{N} - \mathbf{L}) - \frac{1}{2\pi\epsilon}\mathbf{S}'_\kappa(\mathbf{N}^x - \mathbf{L}^x)$

So long as  $\mathbf{Q}$  is symmetric, we can write the derivative of  $E_{\text{pol}}$  with respect to a perturbation  $x$  as

$$E_{\text{pol}}^x = \frac{1}{2}\mathbf{v}_0^\dagger\mathbf{Q}^x\mathbf{v}_0 + \mathbf{q}^\dagger\mathbf{v}_0^x. \quad (3.8)$$

Expanding the first term,

$$\mathbf{v}_0^\dagger\mathbf{Q}^x\mathbf{v}_0 = \mathbf{v}_0^\dagger\mathbf{K}^{-1}(\mathbf{R}^x - \mathbf{K}^x\mathbf{K}^{-1}\mathbf{R})\mathbf{v}_0, \quad (3.9)$$

we have a general expression for the derivative of the reaction-field energy. The matrices  $\mathbf{K}^x$  and  $\mathbf{R}^x$  are given in Table II.

### C. Matrix elements for SWIG discretization

Let us first introduce the matrix elements of the unscreened operators  $\hat{\mathcal{S}}_0$  and  $\hat{\mathcal{D}}_0$ , which are the same as in our previous work.<sup>50</sup> Off-diagonal elements of  $\mathbf{S}_0$ ,  $S_{0,ij}$ , are equal to the unscreened Coulomb interaction between the functions  $g_i(\vec{r})$  and  $g_j(\vec{r})$ . The appropriate Coulomb integral can be written in terms of the error function,

$$S_{0,ij} = \frac{\text{erf}(\zeta_{ij}s_{ij})}{s_{ij}}, \quad (3.10)$$

where  $s_{ij} = |\vec{s}_i - \vec{s}_j|$  and  $\zeta_{ij} = \zeta_i\zeta_j/(\zeta_i^2 + \zeta_j^2)^{1/2}$ . The off-diagonal element  $D_{0,ij}$  is related to  $S_{0,ij}$  according to the relation<sup>17</sup>

$$D_{0,ij} = \vec{n}_j \cdot \frac{\partial S_{0,ij}}{\partial \vec{s}_j}, \quad (3.11)$$

where  $\vec{n}_j$  represents the outward pointing unit vector normal to the cavity surface at the point  $\vec{s}_j$ . Using Eqs. (3.10) and (3.11), one obtains

$$D_{0,ij} = \left( \text{erf}(\zeta_{ij}s_{ij}) - \frac{2\zeta_{ij}s_{ij}}{\sqrt{\pi}}e^{-\zeta_{ij}^2s_{ij}^2} \right) \frac{\vec{n}_j \cdot \vec{s}_{ij}}{s_{ij}^3}. \quad (3.12)$$

In the SWIG approach, diagonal matrix elements  $S_{0,ii}$  are obtained by taking the limit  $s_{ij} \rightarrow 0$  in Eq. (3.10), and furthermore introducing a switching function in the denominator. The resulting definition is

$$S_{0,ii} = \frac{\zeta_i \sqrt{2/\pi}}{F_i}. \quad (3.13)$$

The precise form of the function  $F_i$  can be found in Ref. 50, along with a proof that placing  $F_i$  in the denominator guarantees that the potential energy surface will be smooth, provided that the function  $F_i$  is smooth. The diagonal elements  $D_{0,ii}$  in SWIG are defined by

$$D_{0,ii} = -\frac{S_{0,ii} F_i}{2R_I}, \quad (3.14)$$

where  $R_I$  is the radius of the sphere that contains the point  $\vec{s}_i$ .

Ten-no<sup>68,69</sup> has discussed the evaluation of Gaussian integrals over Yukawa-type potentials and his formulas can be used to evaluate the screened Coulomb interaction between  $g_i(\vec{r})$  and  $g_j(\vec{r})$ . First, we introduce some definitions:

$$T_{ij} = \zeta_{ij} s_{ij}, \quad (3.15a)$$

$$U_{ij} = \frac{\kappa}{2\zeta_{ij}}, \quad (3.15b)$$

$$\alpha_{ij} = e^{-\kappa s_{ij}} \operatorname{erfc}(U_{ij} - T_{ij}), \quad (3.15c)$$

$$\beta_{ij} = e^{\kappa s_{ij}} \operatorname{erfc}(U_{ij} + T_{ij}), \quad (3.15d)$$

$$\alpha'_{ij} = -\kappa \alpha_{ij} + e^{-\kappa s_{ij}} \left( \frac{2\zeta_{ij}}{\sqrt{\pi}} e^{-(U_{ij}-T_{ij})^2} \right), \quad (3.15e)$$

$$\beta'_{ij} = \kappa \beta_{ij} - e^{\kappa s_{ij}} \left( \frac{2\zeta_{ij}}{\sqrt{\pi}} e^{-(U_{ij}+T_{ij})^2} \right). \quad (3.15f)$$

Note that  $\operatorname{erfc}(x) = 1 - \operatorname{erf}(x)$ . The notation in Eq. (3.15) facilitates a succinct expression for the off-diagonal matrix elements of  $S_\kappa$ ,

$$S_{\kappa,ij} = \frac{e^{U_{ij}^2}}{2s_{ij}} (\alpha_{ij} - \beta_{ij}). \quad (3.16)$$

We can use a relation analogous to Eq. (3.11), but replacing  $S_{0,ij}$  with  $S_{\kappa,ij}$  and  $D_{0,ij}$  with  $D_{\kappa,ij}$ , to obtain the off-diagonal elements of  $D_\kappa$ . The result is

$$D_{\kappa,ij} = \left[ \frac{e^{U_{ij}^2}}{2} \left( \frac{\alpha'_{ij} - \beta'_{ij}}{s_{ij}} \right) - \frac{S_{\kappa,ij}}{s_{ij}} \right] \frac{\vec{n}_j \cdot \vec{s}_{ij}}{s_{ij}^3}. \quad (3.17)$$

Analogous to the salt-free case, diagonal elements of  $S_\kappa$  are derived from  $S_{\kappa,ij}$  by taking the limit  $s_{ij} \rightarrow 0$  and introducing  $F_i$  in the denominator:

$$S_{\kappa,ii} = F_i^{-1} [\zeta_i \sqrt{2/\pi} - \kappa \operatorname{erfc}(U_{ii}) \exp(U_{ii}^2)]. \quad (3.18)$$

For  $D_{\kappa,ii}$ , we use a definition analogous to Eq. (3.14):

$$D_{\kappa,ii} = -\frac{S_{\kappa,ii} F_i}{2R_I}. \quad (3.19)$$

Finally, we note that the diagonal elements of  $\mathbf{R}$  should *not* be scaled by  $F_i$ , because this would cancel the factors of  $F_i$  contained in the  $\mathbf{K}$  matrix. Thus, we define an alternative version of  $S_\kappa$ , denoted  $S'_\kappa$ , where the switching function is absent. We can express this as

$$S'_{\kappa,ij} = \begin{cases} S_{\kappa,ij} & \text{for } i \neq j \\ S_{\kappa,ii} F_i & \text{for } i = j \end{cases}. \quad (3.20)$$

The matrix  $S'_\kappa$  is used in place of  $S_\kappa$  in constructing the  $\mathbf{R}$  matrix (see Tables I and II).

## D. Electrostatic potentials and electric fields

To complete the implementation of the screened PCMs, we need to be able to evaluate the screened and unscreened electrostatic potentials and normal electric fields, at each discretization point  $\vec{s}_i$ . For solutes described using quantum mechanics, evaluation of the screened electrostatic potential,  $v_\kappa$ , requires evaluation of Gaussian integrals over a Yukawa-type potential. We have not implemented such integrals in general, owing to the complexity of the formulas involved.<sup>68,69</sup> Therefore, we confine our attention to solutes described at the MM level, for which  $\rho(\vec{r})$  consists of a set of atom-centered point charges,  $\{\rho_J\}$ . In this case, only  $s$ -type Gaussian integrals are required. Analogous to Eq. (3.15), we make the following definitions related to the screened interaction between the point charge  $\rho_J$  (located at position  $\vec{r}_J$ ) and the  $i$ th surface Gaussian,  $g_i(\vec{r})$ :

$$T_{iJ} = \zeta_i r_{iJ}, \quad (3.21a)$$

$$U_i = \frac{\kappa}{2\zeta_i}, \quad (3.21b)$$

$$\alpha_{iJ} = e^{-\kappa r_{iJ}} \operatorname{erfc}(U_i - T_{iJ}), \quad (3.21c)$$

$$\beta_{iJ} = e^{\kappa r_{iJ}} \operatorname{erfc}(U_i + T_{iJ}), \quad (3.21d)$$

$$\alpha'_{iJ} = -\kappa \alpha_{iJ} + e^{-\kappa r_{iJ}} \left( \frac{2\zeta_i}{\sqrt{\pi}} e^{-(U_i - T_{iJ})^2} \right), \quad (3.21e)$$

$$\beta'_{iJ} = \kappa \beta_{iJ} - e^{\kappa r_{iJ}} \left( \frac{2\zeta_i}{\sqrt{\pi}} e^{-(U_i + T_{iJ})^2} \right). \quad (3.21f)$$

Here,  $r_{iJ} = |\vec{s}_i - \vec{r}_J|$ .

The unscreened electrostatic potential due to the point charges  $\{\rho_J\}$ , evaluated at the point  $\vec{s}_i$ , is

$$v_{0,i} = \sum_J \rho_J \frac{\operatorname{erf}(T_{iJ})}{r_{iJ}}. \quad (3.22)$$

The corresponding electric field at  $\vec{s}_i$  is

$$\vec{E}_{0,i} = -\sum_J \rho_J \left( \operatorname{erf}(T_{iJ}) - \frac{2T_{iJ}}{\sqrt{\pi}} e^{-T_{iJ}^2} \right) \frac{\vec{r}_{iJ}}{r_{iJ}^3} \quad (3.23)$$

and the normal component of this field is

$$v_{0,i}^\perp = \vec{n}_i \cdot \vec{E}_{0,i}. \quad (3.24)$$

We next consider how to evaluate the screened electrostatic potential,  $v_\kappa$ , in practical calculations. Unlike  $S_{\kappa,ij}$  (the interaction between surface charges, subject to the screened Coulomb potential), the screened potential  $v_{\kappa,i}$  should account for the existence of an IEL. For the Debye-Hückel model system, the IEL factor [ $\gamma$ , in Eq. (2.3)] fulfills this role, but a simple scaling factor of this type does not exist for an arbitrary cavity shape and distribution of point charges. Therefore, we must make an approximation when computing  $v_\kappa$ .

Our approach is based upon two observations: that the solute cavity is constructed from a union of atom-centered spheres, and that the MM solute consists of point charges located at the centers of these spheres. For an arbitrary MM solute, a crude approximation to  $\phi_\kappa^\rho(\vec{s})$  could be constructed by supposing that the MM charge  $\rho_J$  only makes a contribution to  $\phi_\kappa^\rho(\vec{s})$  for discretization points that lie on the  $J$ th atomic sphere. Under this assumption,  $\phi_\kappa^\rho(\vec{s}_i)$  can always be expressed using Eq. (2.1), for each discretization point  $\vec{s}_i$  and in effect each atom gets its own IEL factor.

In reality, of course, all of the solute charges should contribute to  $\phi_\kappa^\rho$  at each discretization point, but then it is unclear how to account for the IEL. In the spirit of simplicity, we therefore use atomic IEL factors, yet we allow all solute charges to contribute to  $\phi_\kappa^\rho$  across the entire cavity surface. We refer to this as the “local IEL approximation,” and this approximation can be expressed mathematically as

$$\phi_\kappa^\rho(\vec{s}_i) \approx \frac{e^{\kappa R_I}}{1 + \kappa R_I} \int \rho(\vec{r}) \frac{e^{-\kappa|\vec{s}_i - \vec{r}|}}{|\vec{s}_i - \vec{r}|} d^3\vec{r}, \quad (3.25)$$

for all points  $\vec{s}_i$  located on the  $I$ th atomic sphere.

When  $\rho(\vec{r})$  consists of a set of point charges  $\{\rho_J\}$ , the local IEL approximation affords

$$v_{\kappa,i} = \gamma_i \frac{e^{U_i^2}}{2} \sum_J \rho_J \frac{\alpha_{iJ} - \beta_{iJ}}{r_{iJ}}, \quad (3.26)$$

for the screened electrostatic potential at  $\vec{s}_i$ . In this equation, we have defined a “local IEL factor” for the  $i$ th grid point [cf. Eq. (2.3)],

$$\gamma_i = \frac{e^{\kappa R_I}}{1 + \kappa R_I}. \quad (3.27)$$

The screened electric field at  $\vec{s}_i$  can now be evaluated,

$$\vec{E}_{\kappa,i} = -\gamma_i \frac{e^{U_i^2}}{2} \sum_J \rho_J [(\alpha'_{iJ} - \beta'_{iJ})r_{iJ} - (\alpha_{iJ} - \beta_{iJ})] \frac{\vec{r}_{iJ}}{r_{iJ}^3}, \quad (3.28)$$

and its normal component is

$$v_{\kappa,i}^\perp = \vec{n}_i \cdot \vec{E}_{\kappa,i}. \quad (3.29)$$

At this point, the accuracy of the local IEL approximation is unclear, but a number of physical arguments can be made in favor of it. In terms of its physical interpretation, the factor  $\gamma_i$  approximately removes the screening effects in the electrostatic potential,  $v_{\kappa,i}$ , due to mobile solvent ions over a distance of  $R_I$ . That is, mobile solvent ions are not allowed to penetrate between surface point  $\vec{s}_i$  and the source charge

at  $\vec{r}_J$  for a portion  $R_I$  of the total distance  $r_{iJ}$ . Obviously, this is exact for a single point charge centered in a spherical cavity (i.e., the Debye-Hückel model system), and it makes some sense that the nearest and most significant contribution to  $\phi_\kappa^\rho(\vec{s}_i)$  would come from the point charge  $\rho_I$  at the center of the sphere on which the point  $\vec{s}_i$  is located, for which  $\gamma_i$  is accurate given the above physical interpretation. Furthermore, the expression for  $\phi_\kappa^\rho(\vec{s}_i)$  in Eq. (3.25), while approximate for  $\kappa > 0$ , has the correct limit [namely,  $\phi_0^\rho(\vec{s}_i)$ ] as  $\kappa \rightarrow 0$ . Moreover, if  $\kappa R_I \gg 1$  for all atomic spheres, then the integrand in Eq. (3.25) will have significant magnitude only on sphere  $I$ , owing to the factor of  $\exp(-\kappa|\vec{s}_i - \vec{r}|)$  in the integrand.

On the other hand, if  $\kappa R_I \ll 1$  then  $\gamma_i \approx 1$ . Since the use of the LPBE is most appropriate when  $\kappa$  is small, one might question whether these local IEL factors make any difference at all. Numerical tests in Sec. IV will demonstrate not only that the IEL approximation is satisfactory (at least for MM solutes), but also that setting  $\gamma_i = 1$  for each  $i$  affords results that are much *less* satisfactory.

## E. DESMO analytic gradient

In Sec. III B we presented generic expressions for the PCM gradient, in terms of the matrix derivatives  $\mathbf{K}^x$  and  $\mathbf{R}^x$ . At present, we have only implemented these expressions in the DESMO case, so in the interest of brevity we will not present detailed formulas for the the screened IEF-PCM/SS(V)PE analytic gradients. [It should be clear from Table II that the IEF-PCM/SS(V)PE gradient is considerably more complicated than is the DESMO gradient.] Detailed formulas for the DESMO gradient are presented below.

According to Eq. (3.8) and Table II, the necessary components for the DESMO gradient are  $\mathbf{S}_0^x$  and  $\mathbf{M}^x$  as well as the electrostatic potential gradients  $\mathbf{v}_0^x$  and  $\mathbf{v}_\kappa^x$ . We will use the symbol  $\hat{\nabla}_J$  to denote the derivative with respect to displacement of atom  $J$ . Then  $\hat{\nabla}_J v_{0,i}$  is essentially just the negative of the electric field in Eq. (3.23):

$$\hat{\nabla}_J v_{0,i} = \rho_J \left( \text{erf}(T_{iJ}) - \frac{2T_{iJ}}{\sqrt{\pi}} e^{-T_{iJ}^2} \right) \frac{\vec{r}_{iJ}}{r_{iJ}^3} \theta_{iJ}. \quad (3.30)$$

Here,  $\vec{r}_{iJ} = \vec{r}_i - \vec{r}_J$  and

$$\theta_{iJ} = \begin{cases} 0 & \text{if } i \in J \\ 1 & \text{if } i \notin J \end{cases}. \quad (3.31)$$

Similarly, from the electric field in Eq. (3.28) we obtain

$$\hat{\nabla}_J v_{\kappa,i} = \gamma_i \frac{e^{U_i^2}}{2} \rho_J [(\alpha'_{iJ} - \beta'_{iJ})r_{iJ} - (\alpha_{iJ} - \beta_{iJ})] \frac{\vec{r}_{iJ}}{r_{iJ}^3} \theta_{iJ}. \quad (3.32)$$

The gradient  $\mathbf{S}_0^x$ , for off-diagonal elements  $i \neq j$  is

$$\hat{\nabla}_J S_{ij} = - \left( \text{erf}(T_{ij}) - \frac{2T_{ij}}{\sqrt{\pi}} e^{-T_{ij}^2} \right) \frac{\vec{s}_{ij}}{s_{ij}^3} (\theta_{iJ} - \theta_{jJ}), \quad (3.33)$$

and for diagonal elements it is

$$\hat{\nabla}_J S_{ii} = - \frac{S_{ii}}{F_i} \hat{\nabla}_J F_i. \quad (3.34)$$

The gradient of the switching function,  $\hat{\nabla}_J F_i$ , has been reported previously.<sup>50</sup> Notice also that the area derivatives,  $\mathbf{A}^x$  (see Table II) depend only on the switching function gradient, according to Eq. (3.1). Finally, we do not compute  $\mathbf{M}^x$  in practice but instead compute  $\mathbf{M}^x \mathbf{v}_0$ , owing to the simple formula

$$(\hat{\nabla}_J M_{ii}) v_{0,i} = \hat{\nabla}_J v_{\kappa,i} - M_{ii} \hat{\nabla}_J v_{0,i}^x. \quad (3.35)$$

The symmetrization of  $\mathbf{Q}$  as well as the gradient for DESMO can be simplified by defining several sets of charges. First, we define a set of conductor charges

$$\mathbf{q}_\infty = -\mathbf{S}_0^{-1} \mathbf{v}_0, \quad (3.36)$$

that constitute a discretized solution to Eq. (2.19). We also define

$$\mathbf{q}' = \mathbf{S}_0^{-1} \left( \frac{1}{\varepsilon} \mathbf{M} - \mathbf{I} \right) \mathbf{v}_0 \quad (3.37)$$

and

$$\mathbf{q}'' = \left( \mathbf{I} - \frac{1}{\varepsilon} \mathbf{M} \right) \mathbf{q}_\infty. \quad (3.38)$$

Using surface charges  $\mathbf{q} = (\mathbf{q}' + \mathbf{q}'')/2$  is then equivalent to solving Eq. (3.5) with a symmetrized  $\mathbf{Q}$  matrix. In practice, one can obtain the charges  $\mathbf{q}_\infty$ ,  $\mathbf{q}'$ , and  $\mathbf{q}''$  either by explicitly constructing  $\mathbf{S}_0^{-1}$ , or else by solving Eqs. (3.36) and (3.37) separately, using some sort of iterative algorithm. Once  $\mathbf{q}_\infty$  is determined, it is trivial to compute  $\mathbf{q}''$ .

Given the above charges, one can simplify  $E_{\text{pol}}^x$  for the DESMO case to afford

$$E_{\text{pol}}^x = \frac{1}{2} \left( \mathbf{q}_\infty^\dagger \mathbf{S}_0^x \mathbf{q}' - \frac{1}{\varepsilon} \mathbf{q}_\infty^\dagger \mathbf{M}^x \mathbf{v}_0 \right) + \mathbf{q}^\dagger \mathbf{v}_0^x. \quad (3.39)$$

For MM solutes, there is no reason to symmetrize  $\mathbf{Q}$ , and the charges  $\mathbf{q}'$  from Eq. (3.37) can be used in place of  $\mathbf{q}$  to compute both  $E_{\text{pol}}$  and  $E_{\text{pol}}^x$ . This somewhat reduces the computational effort. Similarly, if only the energy (but not the gradient) is required for a DESMO calculation, then it suffices to compute only  $\mathbf{q}''$ , since  $E_{\text{pol}} = \mathbf{v}_0^\dagger \mathbf{q}''/2 = \mathbf{v}_0^\dagger \mathbf{q}''/2$ .

#### IV. NUMERICAL TESTS

We have implemented the DESMO and screened IEF-PCM/SS(V)PE models, for MM solutes only, within a locally-modified version of the Q-Chem software package.<sup>70</sup> This implementation builds upon our recent implementation of smooth PCMs<sup>50–52</sup> and hybrid quantum mechanics/molecular mechanics methods,<sup>71</sup> within this same software. In this section, we present numerical tests of these screened PCMs, both for some simple test cases where an exact analytical solution of the LPBE is available, but also for more realistic MM solutes, where three-dimensional numerical solution of the LPBE provides a benchmark.

For these tests, we employ three different values of the dielectric constant ( $\varepsilon = 4, 20$ , and  $80$ ) and four different Debye lengths ( $\lambda/\text{\AA} = 3, 5, 25$ , and  $\infty$ ). The dielectric constants are chosen to represent three common categories of solvents in chemical applications:  $\varepsilon = 4$  for non-polar organic solvents,

TABLE III. Ionic strengths (in mol/L) for each pair of parameters  $\varepsilon$  and  $\lambda$  explored here, assuming  $T = 298$  K. Note that physiological ionic strengths are  $\sim 0.1$ – $0.2$  mol/L.<sup>72</sup>

$\varepsilon$	$\lambda/\text{\AA}$		
	3	5	25
4	0.0524	0.0189	$7.54 \times 10^{-4}$
20	0.261	0.0943	$3.77 \times 10^{-3}$
80	1.05	0.377	$1.51 \times 10^{-2}$

(benzene, alkanes, ethers),  $\varepsilon = 20$  for polar organic solvents (alcohols, ketones), and  $\varepsilon = 80$  for water. The three Debye lengths are chosen to sample a variety of ionic strengths and to test the local IEL approximation. If the ratio  $R_I/\lambda$  is small, for all atomic spheres, then we expect the local IEL approximation to be satisfactory, but if  $R_I/\lambda \sim 1$ , as it is when  $\lambda = 3$  \AA, then one might expect the local IEL approximation to break down. Note that when  $\lambda = \infty$ , DESMO reduces to GCOSMO/C-PCM and screened IEF-PCM/SS(V)PE reduces to its unscreened form. In Table III, we provide the molar ionic strengths that correspond to each pair of  $\varepsilon$  and  $\lambda$  values used in these tests, at  $T = 298$  K. For  $\lambda = \infty$ , the ionic strength is zero.

For MM solutes, the screened IEF-PCM and screened SS(V)PE methods are equivalent, at the level of integral equations, and we choose to discretize Eq. (2.32) for IEF-PCM/SS(V)PE. We also test a variant of DESMO that we call DESMO-0, which is identical except that we set  $\gamma_i = 1$  in Eq. (3.27), for each  $i$ . In effect, DESMO-0 ignores the IEL and allows mobile solvent ions to penetrate the interior of the solute cavity. Setting  $\gamma_i = 1$  in IEF-PCM/SS(V)PE calculations should not have a significant effect, because  $\mathbf{v}_\kappa$  is absent in this method. More precisely, although  $\phi_\kappa^p$  appears (formally) in Eqs. (2.32) and (2.33), the quantity  $\phi_\kappa^p \equiv 0$  for MM solutes, hence the terms in these equations that involve  $\phi_\kappa^p$  cancel, by virtue of the identity in Eq. (2.34). This explains why, in previous work on screened IEF-PCM and screened SS(V)PE, relatively little attention has been paid to the treatment of the IEL. We will see that this issue is more important in the context of DESMO.

Unless otherwise stated, the solute cavity is constructed using SWIG discretization with 110 Lebedev grid points per atomic sphere. This is sufficient to converge GCOSMO/C-PCM solvation energies to within  $\sim 0.1$  kcal/mol, relative to results obtained using much denser grids.<sup>50</sup>

#### A. Comparison to the Kirkwood model

An analytical solution to the LPBE, for an arbitrary electrostatic multipole centered in a spherical solute cavity, was derived long ago by Kirkwood,<sup>56</sup> and this model can be regarded as a generalization of the Debye-Hückel model problem presented in Sec. II A. Here, we compare exact results for the Kirkwood model to numerical results for various PCMs.

In our first example, we take  $\rho(\vec{r})$  to consist of a single point charge centered in a spherical cavity of radius  $a$ , equivalent to the model in Sec. II A with  $c = 0$ . Numerical results

TABLE IV. Reaction-field energies,  $E_{\text{pol}}$ , for a  $+e$  point charge centered in a cavity of radius 2 Å, along with errors in various PCMs.

$\varepsilon$	$\lambda$ (Å)	$E_{\text{pol}}$ (kcal/mol)	Error (kcal/mol)		
			DESMO	DESMO-0	IEF-PCM/ SS(V)PE
4	$\infty$	-62.262	0.000	0.000	0.000
20	$\infty$	-78.865	0.000	0.000	0.000
80	$\infty$	-81.978	0.000	0.000	0.000
4	25	-63.799	0.000	-0.058	0.000
20	25	-79.173	0.000	-0.012	0.000
80	25	-82.055	0.000	-0.003	0.000
4	5	-68.192	0.003	-0.910	0.000
20	5	-80.051	0.001	-0.182	0.000
80	5	-82.275	0.000	-0.046	0.000
4	3	-76.098	0.007	-1.791	0.000
20	3	-81.632	0.001	-0.358	0.000
80	3	-82.670	0.000	-0.090	0.000

for this model are shown in Tables IV and V for an ion charge of  $+e$  and a cavity radius  $a = 2$  Å. The DESMO and IEF-PCM/SS(V)PE methods are essentially exact for all  $\varepsilon$  and  $\lambda$ , but the same cannot be said for DESMO-0. Although the latter model is accurate  $\lambda = \infty$  (the salt-free limit), its accuracy deteriorates as  $\lambda$  decreases, most notably when  $\varepsilon$  is low. Already, this indicates the importance of accounting for the IEL within DESMO. In fact, the same trends observed for this simplest of models will be seen in many of our subsequent tests.

We next consider a simple model of a highly polar solute. The model consists of two point charges,  $+2e$  and  $-2e$ , separated by a distance of 1 Å, resulting in a dipole moment of  $\mu = 9.6$  debye. We place this system inside a spherical cavity of radius 3.0 Å. The exact energy of this system can be calculated via a multipole expansion of the charge distribution, using Kirkwood's exact formulas for each multipole order.<sup>56</sup> For this example, an expansion up to  $\ell = 7$  is sufficient to converge the energy to within  $10^{-6}$  kcal/mol. Exact results, and errors for various PCMs, are listed in Table VI.

As in the previous example, the screened IEF-PCM/SS(V)PE method is extremely accurate for all values of  $\varepsilon$  and  $\lambda$ . (The  $\approx 0.02$  kcal/mol errors that are listed in Table VI are eliminated if we use 590 Lebedev points to dis-

TABLE V. Salt shifts,  $E_{\text{pol}}(\kappa) - E_{\text{pol}}(\kappa = 0)$ , for a  $+e$  point charge centered in a cavity of radius 2 Å.

$\varepsilon$	$\lambda$ (Å)	Salt shift (kcal/mol)			
		Kirkwood (exact)	DESMO	DESMO-0	IEF-PCM/ SS(V)PE
4	25	-1.54	-1.54	-1.60	-1.54
20	25	-0.31	-0.31	-0.32	-0.31
80	25	-0.08	-0.08	-0.08	-0.08
4	5	-5.93	-5.93	-6.84	-5.93
20	5	-1.19	-1.19	-1.37	-1.19
80	5	-0.30	-0.30	-0.34	-0.30
4	3	-8.30	-8.30	-10.09	-8.30
20	3	-1.66	-1.66	-2.02	-1.66
80	3	-0.42	-0.42	-0.51	-0.42

TABLE VI. Reaction-field energies,  $E_{\text{pol}}$ , for a Kirkwood model of a dipolar solute ( $\mu = 9.6$  debye inside a cavity of radius 3 Å), along with errors in various PCMs.

$\varepsilon$	$\lambda$ (Å)	$E_{\text{pol}}$ (kcal/mol)	Error (kcal/mol)		
			DESMO	DESMO-0	IEF-PCM/ SS(V)PE
4	$\infty$	-16.41	-2.03	-2.03	0.02
20	$\infty$	-22.81	-0.55	-0.55	0.02
80	$\infty$	-24.16	-0.12	-0.12	0.03
4	25	-16.46	-1.98	-2.03	0.02
20	25	-22.83	-0.53	-0.54	0.02
80	25	-24.16	-0.12	-0.12	0.03
4	5	-17.16	-1.28	-2.03	0.02
20	5	-22.99	-0.37	-0.52	0.03
80	5	-24.20	-0.08	-0.12	0.03
4	3	-17.90	-0.52	-2.15	0.02
20	3	-23.17	-0.19	-0.51	0.03
80	3	-24.25	-0.03	-0.11	0.03

cretize each atomic sphere.) DESMO is less accurate than in the previous test, although the largest errors are for  $\varepsilon = 4$ , and for  $\varepsilon = 80$  the errors are  $\leq 0.12$  kcal/mol. However, DESMO does not afford an accurate trend for the “salt shift”, i.e., the difference  $E_{\text{pol}}(\kappa) - E_{\text{pol}}(\kappa = 0)$  at fixed  $\varepsilon$  (see Table VII). In fact, DESMO fails to predict a significant change in  $E_{\text{pol}}$  as the ionic strength changes. In contrast, DESMO-0 affords a correct trend in the salt shift, despite the fact that the errors in  $E_{\text{pol}}$ , relative to exact Kirkwood results, are larger for this method than they are for DESMO.

The failure of DESMO to predict the salt shift in this example indicates that the local IEL approximation may be deficient in cases where solute charges are not located at the centers of the spheres that are used to construct the cavity surface. On the other hand, the salt shifts in this example are quite small ( $< 0.4$  kcal/mol in polar solvents) and are comparable to the errors in the solvation energies themselves. Absolute errors in  $E_{\text{pol}}$  are no larger than 0.6 kcal/mol for  $\varepsilon = 20$ , and the errors in  $E_{\text{pol}}$  are even smaller for test problems with smaller dipole moments. These results seem to indicate that DESMO (and GCOSMO, for  $\kappa = 0$ ) is slightly less accurate than IEF-PCM/SS(V)PE when the atomic charge distribution

TABLE VII. Salt shifts,  $E_{\text{pol}}(\kappa) - E_{\text{pol}}(\kappa = 0)$ , for a Kirkwood model of a dipolar solute ( $\mu = 9.6$  debye inside a cavity of radius 3 Å).

$\varepsilon$	$\lambda$ (Å)	Salt shift (kcal/mol)			
		Kirkwood (exact)	DESMO	DESMO-0	IEF-PCM/ SS(V)PE
4	25	-0.05	0.00	-0.04	-0.05
20	25	-0.01	0.00	-0.01	-0.01
80	25	0.00	0.00	0.00	0.00
4	5	-0.70	0.01	-0.70	-0.69
20	5	-0.18	0.00	-0.15	-0.18
80	5	-0.05	0.00	-0.04	-0.05
4	3	-1.49	0.03	-1.61	-1.49
20	3	-0.35	0.01	-0.32	-0.35
80	3	-0.09	0.00	-0.08	-0.09

is not spherically symmetric. As expected, however, the difference between these methods vanishes as  $\epsilon$  increases.

## B. Comparison to the model of Lotan and Head-Gordon

The second analytical model to which we compare the screened PCMs is the one derived by Lotan and Head-Gordon (LHG).<sup>27</sup> The LHG model generalizes the Kirkwood model and provides an analytic solution to the LPBE for any number of non-overlapping spherical cavities, each of which contains an arbitrary charge density so long as there is no escaped charge. The analytical solution for the solvation energy is lengthy to explicate, and we refer the reader to Ref. 27 for details.

Here, we consider a set of 20 disjoint spherical cavities whose locations are chosen at random within a 30 Å radius of the coordinate origin. The radius of each sphere is selected at random within the range 1.5–2.5 Å, and at the center of each sphere we place a single point charge, selected at random from between  $-e$  and  $+e$ . (All the parameters necessary to define this test system are provided in the supplementary material.<sup>73</sup>) We calculate the electrostatic energy of this system using the formulas in Ref. 27 (with  $\epsilon = 1$  inside each sphere), and compare electrostatic solvation energies (Table VIII) and salt shifts (Table IX) to results computed using various PCMs.

Somewhat surprisingly, we find differences of up to 1.0 kcal/mol between IEF-PCM/SS(V)PE solvation energies and analytic LHG results. (Recall that in the case of the Kirkwood model problems, the IEF-PCM solvation energy differed by no more than 0.03 kcal/mol from the analytical result, and this difference provides a measure of the discretization error.) For the multi-sphere LHG problem, this disagreement persists even when very dense integration grids (up to 5294 points per sphere) are employed. For  $\kappa = 0$ , it is possible to turn off both the switching function and the

TABLE VIII. Reaction-field energies,  $E_{\text{pol}}$ , obtained from the LHG model,<sup>27</sup> for a set of twenty randomly-positioned charges in spherical cavities (see the text for details). PCM results are given in terms of the error relative to the LHG result.

$\epsilon$	$\lambda$ (Å)	$E_{\text{pol}}$ (kcal/mol)	Error (kcal/mol)		
			DESMO	DESMO-0	IEF-PCM/ SS(V)PE
4	$\infty$	-2899.49	-0.01	-0.01	0.98
20	$\infty$	-3672.69	0.00	0.00	0.27
80	$\infty$	-3817.67	0.00	0.00	0.07
4	25	-2914.09	-0.26	-1.39	0.70
20	25	-3675.61	-0.05	-0.28	0.21
80	25	-3818.40	-0.01	-0.07	0.06
4	5	-3035.50	-0.41	-20.92	0.37
20	5	-3699.90	-0.08	-4.18	0.13
80	5	-3824.47	-0.02	-1.04	0.04
4	3	-3122.65	-0.22	-44.47	0.30
20	3	-3717.32	-0.05	-8.90	0.09
80	3	-3828.83	-0.01	-2.22	0.03

TABLE IX. Salt shifts,  $E_{\text{pol}}(\kappa) - E_{\text{pol}}(\kappa = 0)$ , obtained from the LHG model<sup>27</sup> and from various PCMs, for a set of twenty randomly-positioned charges in spherical cavities (see the text for details).

$\epsilon$	$\lambda$ (Å)	Salt shift (kcal/mol)			IEF-PCM/ SS(V)PE
		LHG	DESMO	DESMO-0	
4	25	-14.60	-14.85	-15.99	-14.88
20	25	-2.92	-2.97	-3.20	-2.98
80	25	-0.73	-0.74	-0.80	-0.75
4	5	-136.01	-136.41	-156.93	-136.63
20	5	-27.21	-27.28	-31.39	-27.35
80	5	-6.80	-6.82	-7.85	-6.84
4	3	-223.16	-223.36	-267.62	-223.85
20	3	-44.63	-44.68	-53.52	-44.81
80	3	-11.16	-11.17	-13.38	-11.21

Gaussian blurring in IEF-PCM calculations, but neither of these changes eliminates the discrepancies between IEF-PCM and LHG results. Transposition or symmetrization of the  $\mathbf{K}$  matrix in Table I, as is done in some implementations of IEF-PCM,<sup>51</sup> also fails to eliminate the discrepancies with respect to LHG results.

These results indicate that it is the IEF-PCM/SS(V)PE *ansatz* for the reaction-field potential [Eq. (2.17)] rather than any numerical issue, that is responsible for the diminished accuracy in cases where the cavity consists of disjoint spheres. Chipman has noted that the IEF-PCM/SS(V)PE reaction field is incorrect outside the cavity, if some of the solute charge lies outside the cavity.<sup>23</sup> It follows that when the solute cavity is disjoint, the mutual polarization of the various surface charge distributions may not be described correctly.

To explore this issue further, we consider a system composed of two spheres, one with a radius of 1.29 Å and a point charge of  $-2e$  located at its center, and another with a radius of 1.70 Å and a point charge of  $+1.5e$  located at its center. We take  $\epsilon = 4$  and  $\kappa = 0$  for this calculation, and discretize the two spheres using 194 Lebedev points per sphere, with the SWIG switching function turned off. Figure 2 plots the difference between the IEF-PCM solvation energy and the exact LHG result, as a function of the center-to-center distance between the two spheres. The difference between the two solvation energies disappears quite slowly as a function of distance and exceeds 0.01 kcal/mol even at 10 Å separation. At the same time, this disagreement is typically two or more orders of magnitude smaller than the total reaction-field energy and from a pragmatic chemical standpoint this difference is fairly negligible.

As compared to IEF-PCM/SS(V)PE results, DESMO solvation energies are in much better agreement with analytical LHG results (see Table VIII), and differ by  $< 0.5$  kcal/mol for all values of  $\epsilon$  and  $\lambda$ . When  $\kappa = 0$ , DESMO is equivalent to GCOSMO, and this model reproduces the LHG results (for  $\kappa = 0$ ) to within 0.01 kcal/mol for all values of  $\epsilon$ . Moreover, for the two-sphere example in Fig. 2, the GCOSMO/C-PCM result is virtually identical to the LHG result at all ion-ion distances. Only when the two spheres are nearly in contact with one another does the difference exceed 0.01 kcal/mol.

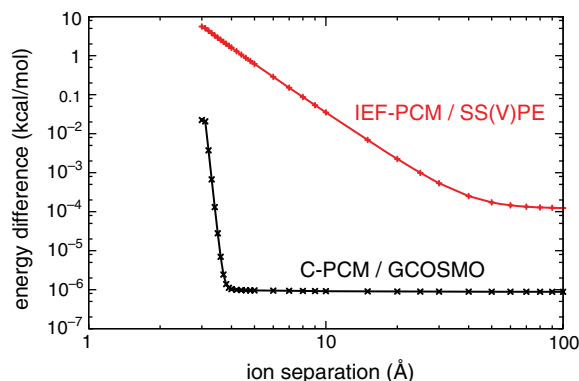


FIG. 2. Difference between the PCM solvation energy and that predicted by the analytic LHG formulas, for two point charges centered in spherical cavities with  $\epsilon = 4$  and  $\kappa = 0$ . The energy difference is plotted as a function of the center-to-center distance between the two spheres, the sum of whose radii is 2.99 Å. (Note that both the horizontal and vertical scales are logarithmic.)

The accuracy of the DESMO-0 model, in contrast, deteriorates as  $\lambda$  decreases, and for  $\epsilon = 4$  the errors are quite large (see Table VIII). This underscores the need to account for the IEL in DESMO calculations, but also indicates that the local IEL approximation appears to be accurate even for cavities composed of disjoint spheres.

### C. Comparison to results from the adaptive Poisson-Boltzmann solver

We next consider more realistic MM solutes and cavity shapes, for which no analytic solution is available. PCM results here will be compared to results obtained by three-dimensional numerical solution of the LPBE, using the so-called adaptive Poisson-Boltzmann solver (APBS),<sup>74</sup> a numerical finite-difference code that performs three-dimensional volumetric integration of the LPBE. Two different solutes are considered: alanine dipeptide and thymine dinucleotide. Atomic charges and radii (i.e., Lennard-Jones “ $\sigma$ ” parameters) are taken from the AMBER99 force field.<sup>75</sup> For the dipeptide example, we construct the cavity using unmodified Lennard-Jones radii, but for the dinucleotide we add a solvent probe radius of 1.4 Å to each Lennard-Jones radius, so that the cavity corresponds to a “solvent accessible surface.”<sup>76</sup> The geometries of the solutes were obtained from the TINKER program<sup>77</sup> and are provided in the supplementary material, along with the atomic charges and radii.<sup>73</sup>

The APBS calculation should provide an accurate result, provided that the integration grid is very dense, and we use a  $193 \times 193 \times 193$  grid, with a grid spacing of 0.05 Å for the dipeptide and 0.10 Å for the dinucleotide. For the Kirkwood model problems in Sec. IV A, these specifications reproduce the total energies to within 0.1 kcal/mol. However, we cannot expect perfect agreement between APBS and the PCM results, even if the latter were exact, because the discretization of the solute cavity is inherently different in these two approaches.

The results of these tests are shown in Tables X–XIII and reflect the same trends seen in the previous tests. The agreement between APBS and the PCMs is remarkably good

TABLE X. Reaction-field energies,  $E_{\text{pol}}$ , for alanine dipeptide, obtained using the APBS software. PCM results are given in terms of the error relative to the APBS result.

$\epsilon$	$\lambda$ (Å)	$E_{\text{pol}}$ (kcal/mol)	Relative energy (kcal/mol)		
			DESMO	DESMO-0	IEF-PCM/ SS(V)PE
4	$\infty$	-66.98	-2.53	-2.53	1.56
20	$\infty$	-87.93	-0.12	-0.12	1.03
80	$\infty$	-92.18	0.66	0.66	0.96
4	25	-67.16	-2.50	-2.56	1.53
20	25	-87.96	-0.11	-0.12	1.02
80	25	-92.19	0.66	0.66	0.96
4	5	-69.59	-2.20	-3.22	1.30
20	5	-88.47	-0.03	-0.24	0.94
80	5	-92.32	0.68	0.63	0.94
4	3	-71.98	-1.91	-4.10	1.14
20	3	-88.97	0.05	-0.39	0.89
80	3	-92.44	0.71	0.60	0.93

TABLE XI. Salt shifts,  $E_{\text{pol}}(\kappa) - E_{\text{pol}}(\kappa = 0)$ , for alanine dipeptide, obtained using the APBS software and various PCMs.

$\epsilon$	$\lambda$ (Å)	Salt shift (kcal/mol)			IEF-PCM/ SS(V)PE
		APBS	DESMO	DESMO-0	
4	25	-0.18	-0.15	-0.21	-0.20
20	25	-0.04	-0.03	-0.04	-0.04
80	25	-0.01	-0.01	-0.01	-0.01
4	5	-2.61	-2.28	-3.30	-2.87
20	5	-0.54	-0.46	-0.66	-0.63
80	5	-0.14	-0.11	-0.17	-0.16
4	3	-5.00	-4.38	-6.58	-5.42
20	3	-1.05	-0.88	-1.32	-1.18
80	3	-0.27	-0.22	-0.33	-0.30

TABLE XII. Reaction-field energies,  $E_{\text{pol}}$ , for thymine dinucleotide, obtained using the APBS software. PCM results are given in terms of the error relative to the APBS result.

$\epsilon$	$\lambda$ (Å)	$E_{\text{pol}}$ (kcal/mol)	Relative energy (kcal/mol)		
			DESMO	DESMO-0	IEF-PCM/ SS(V)PE
4	$\infty$	-27.88	-0.91	-0.91	0.40
20	$\infty$	-36.64	0.17	0.17	0.55
80	$\infty$	-38.41	0.51	0.51	0.60
4	25	-29.25	-0.95	-1.00	0.42
20	25	-36.92	0.17	0.16	0.55
80	25	-38.48	0.51	0.50	0.61
4	5	-32.00	-1.11	-1.77	0.37
20	5	-37.48	0.15	0.02	0.54
80	5	-38.62	0.50	0.47	0.60
4	3	-33.19	-0.98	-2.13	0.33
20	3	-37.74	0.20	0.03	0.53
80	3	-38.69	0.52	0.46	0.60

TABLE XIII. Salt shifts,  $E_{\text{pol}}(\kappa) - E_{\text{pol}}(\kappa = 0)$ , for thymine dinucleotide, obtained using the APBS software and various PCMs.

$\epsilon$	$\lambda$ (Å)	Salt shift (kcal/mol)			IEF-PCM/ SS(V)PE
		APBS	DESMO	DESMO-0	
4	25	-1.37	-1.41	-1.46	-1.35
20	25	-0.27	-0.28	-0.29	-0.27
80	25	-0.07	-0.07	-0.07	-0.07
4	5	-4.12	-4.31	-4.98	-4.15
20	5	-0.84	-0.86	-1.00	-0.85
80	5	-0.21	-0.22	-0.25	-0.21
4	3	-5.31	-5.39	-6.53	-5.39
20	3	-1.10	-1.08	-1.31	-1.12
80	3	-0.28	-0.27	-0.33	-0.28

( $\sim 1$  kcal/mol or better) considering that they are significantly different approaches. For  $\epsilon = 4$ , the DESMO results for  $E_{\text{pol}}$  differ from APBS by 1–2 kcal/mol, but the differences are much smaller in the higher-dielectric environments. This indicates that the local IEL approximation fares well even for complicated cavity shapes and non-trivial solute charge distributions. Curiously, for  $\epsilon = 80$ , the DESMO and DESMO-0 models are in excellent agreement here, which was not the case in previous tests.

## V. SUMMARY

We have formulated a new boundary-element PCM for electrolytic solvents that we call the Debye-Hückel-like screening model, or DESMO. This model generalizes COSMO to solutions with non-zero ionic strength, within the Debye-Hückel (linearized Poisson-Boltzmann) limit. DESMO is closely related to “screened” versions of the PCMs known as IEF-PCM and SS(V)PE that have previously been developed for electrolytes.<sup>23,42,43</sup> Similar to COSMO in the salt-free case, however, DESMO is significantly simpler to implement and much less expensive to evaluate, as compared to these alternative PCMs.

We have also presented the first fully analytic implementation of the screened IEF-PCM/SS(V)PE model. This implementation builds upon our “SWIG” method for smooth discretization of the integral equations that appear in boundary-element PCMs,<sup>50,52</sup> and our implementation of these screened PCMs is the first that is amenable to analytic gradient techniques. For single-cavity problems, the IEF-PCM/SS(V)PE approach affords the same solvation energy as does the LPBE, but for systems composed of disjoint cavities, we observe small discrepancies between the screened IEF-PCM/SS(V)PE solvation energy and that obtained by exact solution of the LPBE. We ascribe these differences to a fundamental limitation of the PCM reaction-field *ansatz*.

For solutes described by molecular mechanics point charges, we have shown that DESMO accurately approximates the exact solution of the LPBE, in cases where the exact solution is available, and accurately approximates other numerical solutions in cases where no analytic solution is available. For polar solvents (modeled here using  $\epsilon = 20$

and 80), the total energies predicted by DESMO lie within  $\sim 0.5$  kcal/mol of benchmark results, across a broad range of ionic strengths. To obtain this level of accuracy, an approximate treatment of the ion exclusion layer appears to be mandatory, and use of the “DESMO-0” model (which neglects the IEL and was introduced here solely for comparative purposes) is *not* recommended. Further refinements to the treatment of the IEL, beyond the “local IEL approximation” that is introduced here, may improve the accuracy of DESMO.

Given the accuracy, simplicity, and computational efficiency of DESMO, we think that this model represents an important addition to the PCM toolbox.

## ACKNOWLEDGEMENT

We thank Teresa Head-Gordon for comments on the manuscript. This work was supported by an NSF CAREER award (CHE-0748448). Calculations were performed at the Ohio Supercomputer Center (project no. PAS-0291). J.M.H. is an Alfred P. Sloan Foundation fellow.

<sup>1</sup>A. Warshel and J. Åqvist, *Annu. Rev. Biophys. Biophys. Chem.* **20**, 267 (1991).

<sup>2</sup>B. Honig and A. Nicholls, *Science* **268**, 1144 (1995).

<sup>3</sup>D. Bashford and D. A. Case, *Annu. Rev. Phys. Chem.* **51**, 129 (2000).

<sup>4</sup>M. Feig and C. L. Brooks III, *Curr. Opin. Struct. Biol.* **14**, 217 (2004).

<sup>5</sup>N. A. Baker, *Methods. Enzymol.* **383**, 94 (2004).

<sup>6</sup>N. A. Baker, *Curr. Opin. Struct. Biol.* **15**, 137 (2005).

<sup>7</sup>A. Warshel, P. K. Sharma, M. Kato, and W. W. Parson, *Biochim. Biophys. Acta* **1764**, 1647 (2006).

<sup>8</sup>P. Grochowski and J. Trylska, *Biopolymers* **89**, 93 (2008).

<sup>9</sup>B. Z. Lu, Y. C. Zhou, M. J. Holst, and J. A. McCammon, *Comm. Comp. Phys.* **3**, 973 (2008).

<sup>10</sup>J. Wang, C. Tan, Y.-H. Tan, Q. Lu, and R. Luo, *Commun. Comput. Phys.* **3**, 1010 (2008).

<sup>11</sup>A. Onufriev, *Annu. Rep. Comp. Chem.* **4**, 125 (2008).

<sup>12</sup>A. Onufriev, in *Modeling Solvent Environments: Applications to Simulations of Biomolecules*, edited by M. Feig (Wiley-VCH, Hoboken, 2010), Chap. VI, pp. 127–165.

<sup>13</sup>F. Marchand and A. Caffisch, in *Modeling Solvent Environments: Applications to Simulations of Biomolecules*, edited by M. Feig (Wiley-VCH, Hoboken, 2010), Chap. IX, pp. 209–232.

<sup>14</sup>E.-H. Yap and T. Head-Gordon, *J. Chem. Theory Comput.* **6**, 2214 (2010).

<sup>15</sup>C. Amovilli, V. Barone, R. Cammi, E. Cancés, M. Cossi, B. Mennucci, C. S. Pomelli, and J. Tomasi, *Adv. Quantum Chem.* **32**, 227 (1999).

<sup>16</sup>R. Cammi, B. Mennucci, and J. Tomasi, in *Computational Chemistry: Reviews of Current Trends*, edited by J. Leszczynski (World Scientific, Singapore, 2003), Vol. 8, Chap. I, pp. 1–79.

<sup>17</sup>J. Tomasi, B. Mennucci, and R. Cammi, *Chem. Rev.* **105**, 2999 (2005).

<sup>18</sup>C. J. Cramer and D. G. Truhlar, *Chem. Rev.* **99**, 2161 (1999).

<sup>19</sup>C. J. Cramer and D. G. Truhlar, in *Trends and Perspectives in Modern Computational Science*, edited by G. Maroulis and T. E. Simos, *Lecture Series on Computer and Computational Sciences* (Brill/VSP, Leiden, 2006), Vol. 6, pp. 112–140.

<sup>20</sup>C. J. Cramer and D. G. Truhlar, *Acc. Chem. Res.* **41**, 760 (2008).

<sup>21</sup>A. Papazyan and A. Warshel, *J. Phys. Chem. B* **101**, 11254 (1997).

<sup>22</sup>W. W. Parson and A. Warshel, in *Biophysical Techniques in Photosynthesis*, edited by T. J. Aartsma and J. Matysik (Springer, New York, 2008), Vol. 2, Chap. XX, pp. 401–420.

<sup>23</sup>D. M. Chipman, *J. Chem. Phys.* **120**, 5566 (2004).

<sup>24</sup>A. Warshel and S. T. Russell, *Q. Rev. Biophys.* **17**, 283 (1984).

<sup>25</sup>Y. Y. Sham, Z. T. Chu, and A. Warshel, *J. Phys. Chem. B* **101**, 4458 (1997).

<sup>26</sup>M. J. Schnieders, N. A. Baker, P. Ren, and J. W. Ponder, *J. Chem. Phys.* **126**, 124114 (2007).

<sup>27</sup>I. Lotan and T. Head-Gordon, *J. Chem. Theory Comput.* **2**, 541 (2006).

<sup>28</sup>B. J. Klein and G. R. Pack, *Biopolymers* **22**, 2331 (1983).

<sup>29</sup>M. J. Holst and F. Saied, *J. Comput. Chem.* **16**, 337 (1995).

- <sup>30</sup>R. Gargallo, P. H. Hünenberger, F. X. Avilés, and B. Oliva, *Protein Sci.* **12**, 2161 (2003).
- <sup>31</sup>M. Feig, A. Onufriev, M. S. Lee, W. Im, D. A. Case, and C. L. Brooks III, *J. Comput. Chem.* **25**, 265 (2004).
- <sup>32</sup>T. Z. Lwin, R. Zhou, and R. Luo, *J. Chem. Phys.* **124**, 034902 (2006).
- <sup>33</sup>C. Tan, L. Yang, and R. Luo, *J. Phys. Chem. B* **110**, 18680 (2006).
- <sup>34</sup>J. Wang, C. Tan, E. Chanco, and R. Luo, *Phys. Chem. Chem. Phys.* **12**, 1194 (2010).
- <sup>35</sup>J. Wang and R. Luo, *J. Comput. Chem.* **31**, 1689 (2010).
- <sup>36</sup>T. Hou, J. Wang, Y. Li, and W. Wang, *J. Comput. Chem.* **32**, 866 (2011).
- <sup>37</sup>J. Wang, Q. Cai, Z.-L. Li, H.-K. Zhao, and R. Luo, *Chem. Phys. Lett.* **468**, 112 (2009).
- <sup>38</sup>A. Klamt and G. Schüürmann, *J. Chem. Soc., Perkin Trans. 2*, 799 (1993).
- <sup>39</sup>T. N. Truong and E. V. Stefanovich, *Chem. Phys. Lett.* **240**, 253 (1995).
- <sup>40</sup>T. N. Truong, U. N. Nguyen, and E. V. Stefanovich, *Int. J. Quantum Chem., Symp.* **30**, 1615 (1996).
- <sup>41</sup>V. Barone and M. Cossi, *J. Phys. Chem. A* **102**, 1995 (1998).
- <sup>42</sup>E. Cancès, B. Mennucci, and J. Tomasi, *J. Chem. Phys.* **107**, 3032 (1997).
- <sup>43</sup>B. Mennucci, E. Cancès, and J. Tomasi, *J. Phys. Chem. B* **101**, 10506 (1997).
- <sup>44</sup>B. Mennucci, R. Cammi, and J. Tomasi, *J. Chem. Phys.* **109**, 2798 (1998).
- <sup>45</sup>J. Tomasi, B. Mennucci, and E. Cancès, *J. Mol. Struct.: THEOCHEM* **464**, 211 (1999).
- <sup>46</sup>E. Cancès, in *Continuum Solvation Models in Chemical Physics*, edited by B. Mennucci and R. Cammi (Wiley, New York, 2007), pp. 29–48.
- <sup>47</sup>D. M. Chipman, *J. Chem. Phys.* **112**, 5558 (2000).
- <sup>48</sup>E. Cancès and B. Mennucci, *J. Chem. Phys.* **114**, 4744 (2001).
- <sup>49</sup>D. M. Chipman, *Theor. Chem. Acc.* **107**, 80 (2002).
- <sup>50</sup>A. W. Lange and J. M. Herbert, *J. Chem. Phys.* **133**, 244111 (2010).
- <sup>51</sup>A. W. Lange and J. M. Herbert, “Symmetric versus asymmetric discretization of the integral equations in polarizable continuum solvation models,” *Chem. Phys. Lett.* (in press).
- <sup>52</sup>A. W. Lange and J. M. Herbert, *J. Phys. Chem. Lett.* **1**, 556 (2010).
- <sup>53</sup>P. Debye and E. Hückel, *Phys. Z.* **24**, 185 (1923).
- <sup>54</sup>P. Debye and E. Hückel, in *Collected Papers of Peter J. W. Debye* (Interscience Publishers, New York, 1954), pp. 217–263.
- <sup>55</sup>M. J. Holst, “The Poisson-Boltzmann Equation: Analysis and Multi-level Numerical Solution,” PhD thesis, University of Illinois at Urbana-Champaign, 1994.
- <sup>56</sup>J. G. Kirkwood, *J. Chem. Phys.* **2**, 351 (1934).
- <sup>57</sup>M. Born, *Phys. Z.* **1**, 45 (1920).
- <sup>58</sup>V. Luzhkov and A. Warshel, *J. Comput. Chem.* **13**, 199 (1992).
- <sup>59</sup>A. Papazyan and A. Warshel, *J. Chem. Phys.* **107**, 7975 (1997).
- <sup>60</sup>J. L. Rivail, B. Terryn, D. Rinaldi, and M. F. Ruiz-Lopez, *J. Mol. Struct.: THEOCHEM* **120**, 387 (1985).
- <sup>61</sup>J. B. Foresman, T. A. Keith, K. B. Wiberg, J. Snoonian, and M. J. Frisch, *J. Phys. Chem.* **100**, 16098 (1996).
- <sup>62</sup>D. M. Chipman and M. Dupuis, *Theor. Chem. Acc.* **107**, 90 (2002).
- <sup>63</sup>B. Ginovska, D. M. Camaioni, M. Dupuis, C. A. Schwerdtfeger, and Q. Gil, *J. Phys. Chem. A* **112**, 10604 (2008).
- <sup>64</sup>V. I. Lebedev, *USSR Comput. Math. Math. Phys.* **15**, 44 (1975).
- <sup>65</sup>D. M. York and M. Karplus, *J. Phys. Chem. A* **103**, 11060 (1999).
- <sup>66</sup>B. A. Gregersen and D. M. York, *J. Chem. Phys.* **122**, 194110 (2005).
- <sup>67</sup>M. Cossi, G. Scalmani, N. Rega, and V. Barone, *J. Chem. Phys.* **117**, 43 (2002).
- <sup>68</sup>S. Ten-no, *Chem. Phys. Lett.* **398**, 56 (2004).
- <sup>69</sup>S. Ten-no, *J. Chem. Phys.* **126**, 014108 (2007).
- <sup>70</sup>Y. Shao, L. Fusti-Molnar, Y. Jung, J. Kussmann, C. Ochsenfeld, S. T. Brown, A. T. B. Gilbert, L. V. Slipchenko, S. V. Levchenko, D. P. O’Neill, R. A. DiStasio Jr., R. C. Lochan, T. Wang, G. J. O. Beran, N. A. Besley, J. M. Herbert, C. Y. Lin, T. Van Voorhis, S. H. Chien, A. Sodt, R. P. Steele, V. A. Rassolov, P. E. Maslen, P. P. Korambath, R. D. Adamson, B. Austin, J. Baker, E. F. C. Byrd, H. Dachsel, R. J. Doerksen, A. Dreuw, B. D. Dunietz, A. D. Dutoi, T. R. Furlani, S. R. Gwaltney, A. Heyden, S. Hirata, C.-P. Hsu, G. Kedziora, R. Z. Khalliulin, P. Klunzinger, A. M. Lee, M. S. Lee, W. Liang, I. Lotan, N. Nair, B. Peters, E. I. Proynov, P. A. Pieniazek, Y. M. Rhee, J. Ritchie, E. Rosta, C. D. Sherrill, A. C. Simmonett, J. E. Subotnik, H. L. Woodcock III, W. Zhang, A. T. Bell, A. K. Chakraborty, D. M. Chipman, F. J. Keil, A. Warshel, W. J. Hehre, H. F. Schaefer III, J. Kong, A. I. Krylov, P. M. W. Gill, and M. Head-Gordon, *Phys. Chem. Chem. Phys.* **8**, 3172 (2006).
- <sup>71</sup>A. W. Lange and J. M. Herbert, *J. Am. Chem. Soc.* **131**, 3913 (2009).
- <sup>72</sup>R. K. Scopes, *Protein Purification: Principles and Practice* (Springer-Verlag, New York, 1994).
- <sup>73</sup>See supplementary material at <http://dx.doi.org/10.1063/1.3592372> for a tabulation of parameters that define the test problems.
- <sup>74</sup>N. A. Baker, D. Sept, S. Joseph, M. J. Holst, and J. A. McCammon, *Proc. Natl. Acad. Sci. U.S.A.* **98**, 10037 (2001).
- <sup>75</sup>J. Wang, P. Cieplak, and P. A. Kollman, *J. Comput. Chem.* **21**, 1049 (2000).
- <sup>76</sup>B. Lee and F. M. Richards, *J. Mol. Biol.* **55**, 379 (1971).
- <sup>77</sup>TINKER, version 4.2, <http://dasher.wustl.edu/tinker>.